

Periodic Topological Deep Learning for Polymer Design and Discovery

Yasharth Yadav,¹ Tze Kwang Gerald Er,² Atsushi Goto,² and Kelin Xia^{1,*}

¹*School of Physical and Mathematical Sciences, Nanyang Technological University, Singapore 637371*

²*School of Chemistry, Chemical Engineering and Biotechnology (CCEB),
Nanyang Technological University, Singapore 637371*

Polymers underpin applications across energy, healthcare, and materials science, yet their vast chemical space makes systematic discovery challenging. Most machine learning approaches represent polymers as molecular graphs of a single repeating unit, thereby missing both the periodicity of polymer chains and many-body interactions beyond pairwise bonds. We introduce Periodic-TDL, a deep learning framework built on periodic Vietoris-Rips complexes that capture many-body interactions across multiple spatial scales, followed by a hierarchical simplicial message-passing (HSMP) encoder that propagates information from long-range interactions to covalent bonds, yielding representations enriched by higher-order topological features. Periodic-TDL outperforms all state-of-the-art models across polymer property prediction tasks spanning electronic, optical, physical, and thermal targets. Furthermore, we quantitatively validate how ester-to-amide substitution and α -methylation enhance thermal stability. Using a computationally synthesized dataset of 48,208 structures-generated via systematic substitution of acrylate and acrylamide polymers-we observed a mean T_g increase of $\sim 55^\circ\text{C}$ for ester-to-amide substitutions and $\sim 14^\circ\text{C}$ for backbone α -methylation across matched polymer pairs. To verify these predicted trends, we use our Periodic-TDL model to analyze six novel polymer pairs from independent experimental measurements, including three newly synthesized polymers previously unreported in the literature. The experimental data successfully confirmed the model’s predictions. Ultimately, these findings demonstrate that Periodic-TDL captures the underlying physical effects of specific functional group modifications, rather than merely optimizing predictive performance on benchmark datasets.

Keywords: Polymer Property Prediction, Topological Deep Learning, Simplicial Message Passing, Polymer Informatics, Structure–Property Relationships

INTRODUCTION

Polymers underpin modern life across electronics, aerospace, energy, and healthcare [1–3], owing to their tunable thermal, electronic, mechanical, and optical properties. This tunability arises from a virtually infinite chemical space that can be navigated by modifying their molecular architecture and functional group chemistry [4, 5]. While the intuition of polymer chemists remains invaluable, the sheer scale of this space renders purely experimental discovery impractical [6]. Polymer informatics has emerged to address this challenge by applying modern tools from data science and machine learning, enabling substantial progress in both property prediction and inverse design, where polymers meeting prescribed requirements are identified [7–11].

Central to any machine learning approach is the choice of how polymer structure is encoded. Early methods derived hand-crafted numerical vectors from local atomic environments, functional groups, and packing descriptors [12–15]. With the rise of deep learning, the field shifted toward learning directly from machine-readable molecular representations, where numerical vectors emerge as an implicit outcome of the neural encoder. This shift places the burden of accuracy squarely on the representation itself, which must provide a faithful and complete description of the molecular structure for the encoder to extract meaningful information. Sequence-based Transformers [16–18] treat the SMILES string [19] as a chemical language, pretraining on large unlabelled corpora before fine-tuning on labelled property datasets. Message-passing neural networks [20–28] learn from molecular graphs describing covalent connectivity. Multimodal frameworks [29–32] combine different representation types to compensate for the blind spots of any single modality. Despite this diversity, most deep learning frameworks construct their structural input from a single, finite repeating unit. As a result, they effectively treat polymers as small molecules rather than as macromolecules, creating a fundamental representational bottleneck that remains largely unaddressed [33–35].

Unlike small molecules with a fixed number of atoms, polymers consist of periodic chains of repeating chemical subunits that can extend to millions of atoms, with potentially complex architectures [36]. A faithful representation must therefore structural relationships that span adjacent repeating units in a polymer. Several works have recognised this and proposed periodic graph representations as a more suitable alternative. The wDMPNN framework [25], the

* xiakelin@ntu.edu.sg

periodic polymer graph [24], and PolyGNN [28] all construct graph representations that extend beyond a single repeating unit to capture inter-unit connectivity under periodic boundary conditions. However, these approaches share two fundamental limitations. First, graph representations are inherently restricted to pairwise interactions and cannot capture the many-body structure arising from three or more atoms simultaneously. Second, message passing operates only at the scale of covalent bonds, missing long-range non-covalent interactions that are critical for bulk polymer properties. These limitations call for a richer representational framework that can explicitly encode many-body interactions across multiple spatial scales.

More recently, topological deep learning (TDL) has emerged as a principled extension of graph neural networks that addresses their fundamental restriction to pairwise interactions [37–40]. Rather than representing molecular structure as a graph of atoms and bonds, TDL operates on richer topological domains that can natively encode many-body interactions among three or more elements simultaneously. The most widely studied of these are simplicial complexes, which are generalizations of graphs capable of encoding interactions between multiple atoms through higher-dimensional simplices [41–43]. Other structures, including cell complexes [44], sheaves [45], and hypergraphs [46], are also gaining traction. Message passing schemes defined across these structures enable information exchange between objects of varying dimension. This allows representations to incorporate both local and global structural information [47–50]. These capabilities have demonstrated considerable success in molecular property prediction [51–55]. However, no existing TDL framework incorporates the periodic nature of polymers, where chains are still treated as finite molecular fragments, discarding the key structural aspect that distinguishes polymers from small molecules.

Here we introduce Periodic-TDL, a framework that captures both periodicity and higher-order interactions across multiple spatial scales. At its core is the *periodic Vietoris–Rips complex* representation of polymers, which encodes interactions between atoms across adjacent repeating units under periodic boundary conditions, representing both covalent and non-covalent interactions through higher-dimensional simplices. To learn from this representation, we develop the *Hierarchical Simplicial Message Passing (HSMP)* encoder, which operates over a nested sequence of simplicial complexes and propagates information from coarser to finer scales in a chemically motivated direction. Notably, at the finest filtration level, HSMP reduces to a standard molecular graph, enabling direct integration into established self-supervised pretraining pipelines [22, 56–60] designed for conventional graph encoders. This compatibility is particularly valuable given the scarcity of labelled polymer data. To equip higher-order simplices with meaningful features, we further introduce curvature-based featurization using Forman’s discretization of Ricci curvature [44], which generalizes naturally to simplices of any dimension. Next, we pretrained Periodic-TDL on one million unlabelled polymers and evaluated its performance across nine polymer properties spanning electronic, optical, physical, and thermal targets. Finally, we applied Periodic-TDL to a computationally generated dataset of 48208 systematically substituted polymers from acrylate and acrylamide families. Specifically, we studied the effects of ester-to-amide substitution and backbone α -methylation on the glass transition temperature (T_g) of these polymers. To ensure the chemical credibility of our model, we compared the predicted T_g changes against six polymer pairs spanning eight polymers from prior experimental studies and three newly synthesized polymers.

RESULTS

Periodic Vietoris–Rips Filtration Captures Topology Beyond a Single Repeating Unit

We represent linear homopolymers using a periodic Vietoris–Rips complex that formally encodes topological relationships between atoms belonging to adjacent repeating units. Technical details of our construction are provided in the Methods section. Here, we illustrate the core ideas using poly(bisphenol A carbonate) as a representative example.

Figure 1(a) shows the repeating unit of poly (bisphenol A carbonate) and its corresponding three-dimensional atomic point cloud. A pairwise Euclidean distance matrix constructed from this point cloud [Figure 1(b)] encodes spatial proximity only within a single arbitrarily chosen unit, failing to account for translational symmetry along the polymer backbone. This limitation is particularly evident at the boundaries, where atoms belonging to the carbonate linkage appear spatially distant simply because they reside at opposite ends of the chosen unit, despite being directly connected in the actual polymer. To resolve this, we construct a periodic distance matrix by incorporating translated copies of the repeating unit via iterative rearrangement of backbone fragments while strictly preserving chemical connectivity [61], defining each interatomic distance as the minimum separation across all translated copies.

From this periodic distance matrix, multi-scale topological structure is extracted via Vietoris–Rips filtration [41, 42]. For a given cutoff ϵ_i , any set of $k + 1$ atoms with all pairwise distances below ϵ_i gives rise to a k -simplex, and the resulting simplicial complex $\text{VR}_{\epsilon_i}(\mathbf{D})$ acts as a higher-dimensional generalization of a graph. Progressively increasing ϵ_i incorporates interactions over increasing spatial ranges, capturing both covalent and non-covalent interactions [62]. Simplicial complexes and Vietoris–Rips filtration are formally defined in Supplementary Information.

Figure 1(c) compares Vietoris–Rips filtration constructed using the non-periodic (intra-monomer) distance matrix

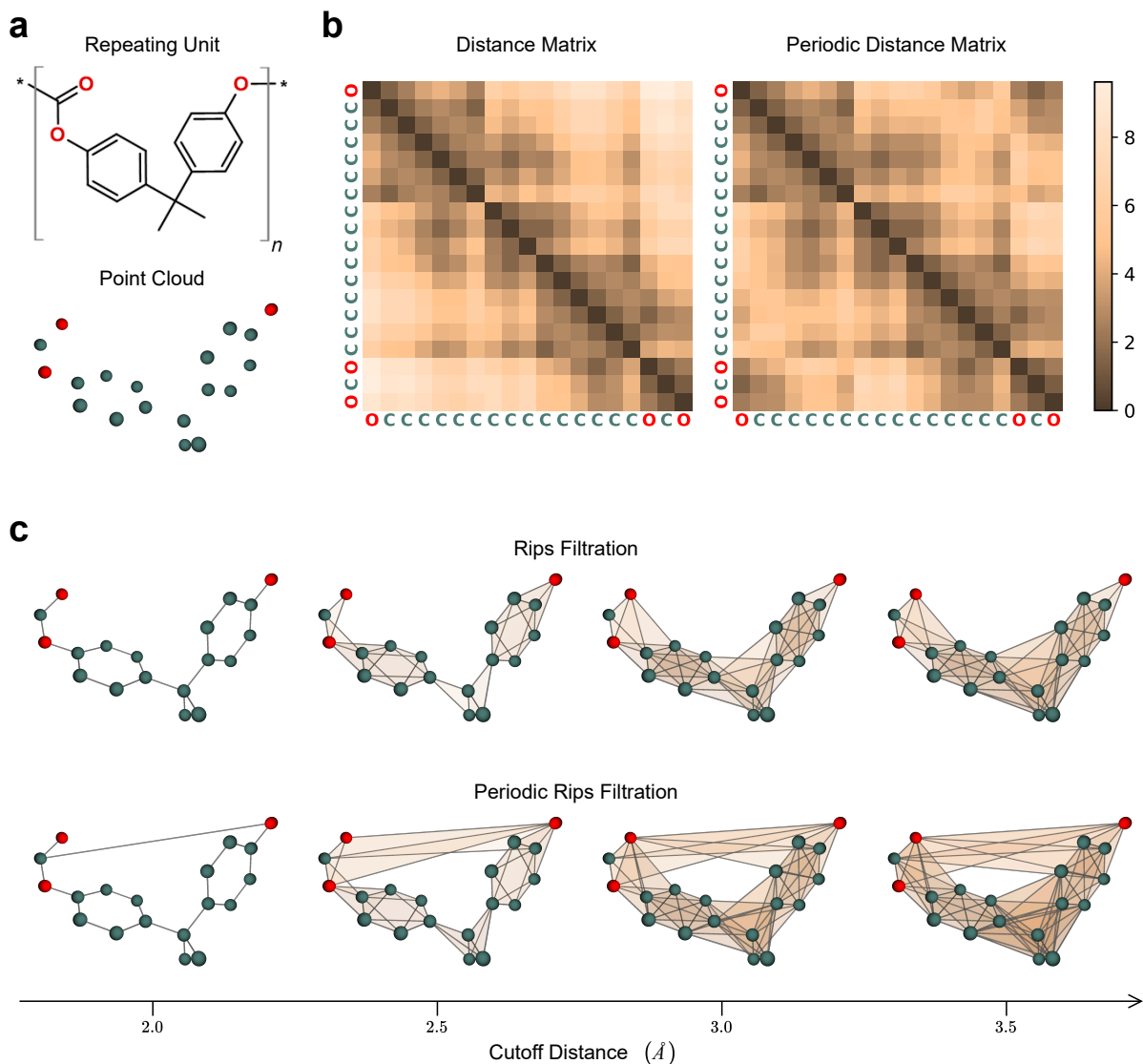


FIG. 1. **Periodic Vietoris–Rips complex representation of poly (bisphenol A carbonate).** (a) Repeating unit of poly (bisphenol A carbonate), together with its corresponding three-dimensional atomic point cloud. (b) Pairwise distance matrices computed from a single repeating unit (left, intra-monomer distance matrix) and from its translated copies (right, periodic distance matrix). The periodic distance matrix restores the correct spatial proximity between atoms that lie near the boundaries of a chosen repeating unit but are adjacent in the actual polymer. (c) Comparison of Vietoris–Rips filtration constructed using the intra-monomer distance matrix (top row) and the periodic distance matrix (bottom row) at increasing cutoff distances.

and the periodic distance matrix. In both cases the same filtration procedure is applied, but the underlying distance matrices differ, leading to distinct simplicial complexes. In the non-periodic representation, atoms located near the boundaries of the chosen repeating unit appear spatially distant and therefore remain disconnected at small cutoffs. In contrast, the periodic distance matrix restores the correct spatial proximity between atoms belonging to adjacent repeating units, yielding a Vietoris–Rips complex that reflects the connectivity of the extended polymer and is invariant to the arbitrary choice of repeating unit. At $\epsilon_i = 2\text{\AA}$, the resulting complexes recover covalent bonds. In the non-periodic case, these correspond only to bonds within a single repeating unit, whereas the periodic Vietoris–Rips complex captures covalent bonds across repeating units along the polymer backbone. At cutoffs of $\epsilon_i = 2.5\text{\AA}$ and beyond, higher-dimensional simplices begin to appear, reflecting many-body interactions. These simplicial complexes grow denser at larger cutoffs as more atoms fall within mutual proximity. Thus, the periodic Vietoris–Rips filtration accurately represents the topological structure of a polymer chain while systematically incorporating multi-body interactions across varying spatial scales

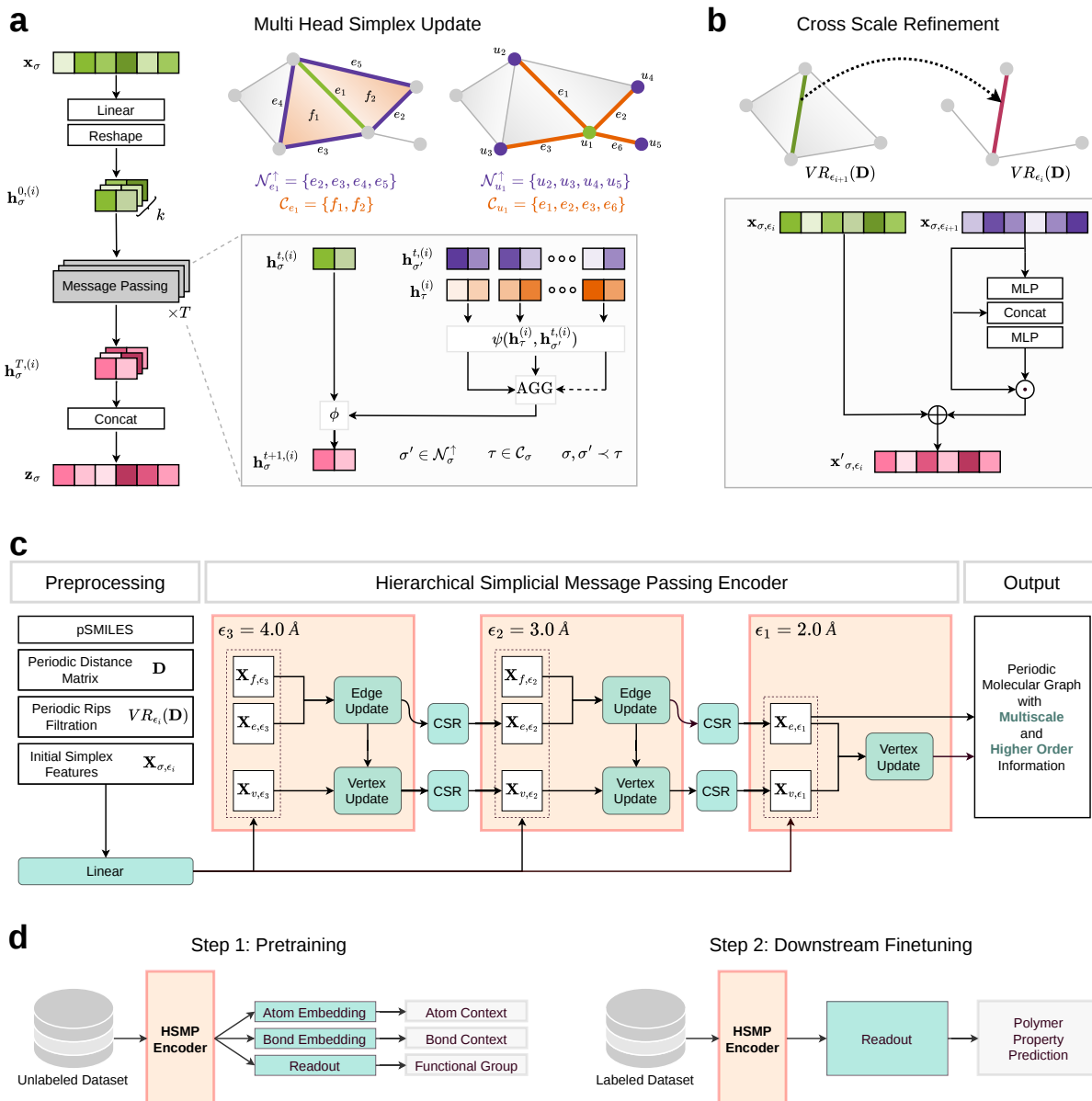


FIG. 2. **Overview of hierarchical simplicial message passing.** (a) Multi-head simplicial message passing at a fixed filtration level $VR_{\epsilon_i}(\mathbf{D})$, where simplex features are projected, split into multiple heads, updated via upper-adjacency (coface-mediated) message passing, and concatenated. (b) Cross-scale refinement between consecutive filtration levels $VR_{\epsilon_{i+1}} \rightarrow VR_{\epsilon_i}$, where coarse-scale simplex representations modulate finer-scale features through a residual gated mechanism. (c) The full HSMP pipeline operating over the Vietoris–Rips filtration, combining within-level simplicial message passing and cross-scale refinement across multiple cutoffs, proceeding from coarser to finer spatial scales. (d) Pretraining and fine-tuning pipelines, where the encoder is pretrained using atom context, bond context, and functional group prediction tasks at the finest level ϵ_1 , and finetuned by global mean pooling of atom embeddings for downstream polymer property prediction.

HSMP Learns Across Simplex Dimensions and Filtration Scales

We develop the *hierarchical simplicial message passing (HSMP) encoder* as a learning component of Periodic-TDL, designed to operate directly on the periodic Vietoris–Rips complex constructed above. Since a Vietoris–Rips complex explicitly includes simplices of multiple dimensions arising from a filtration across varying spatial scales, the HSMP encoder operates both within and across individual filtration levels, enabling the integration of multi-scale interactions in a principled manner.

Multi-head simplicial message passing

We extend the Message Passing Simplicial Network framework of Bodnar et al. [47] to a multi-head setting, allowing multiple parallel simplex updates that operate on different representation subspaces to capture complementary interaction patterns [47, 63, 64]. At a given filtration parameter, let $\sigma \in \text{VR}_{\epsilon_i}(\mathbf{D})$ be a simplex with feature \mathbf{x}_σ . As illustrated in Figure 2(a), \mathbf{x}_σ is projected and split into k parallel representations $\mathbf{h}_\sigma^{0,(i)} \in \mathbb{R}^{D/k}$, each processed independently through a T -layer message passing module and concatenated to yield the updated representation \mathbf{z}_σ .

Each message passing layer aggregates over the upper-adjacent neighborhood of σ , defined via the boundary incidence relation \prec , where $\sigma \prec \tau$ if $\sigma \subset \tau$ and there exists no δ such that $\sigma \subset \delta \subset \tau$. The co-boundary and upper-adjacent sets of σ are respectively

$$\begin{aligned} \mathcal{C}_\sigma &= \{\tau \mid \sigma \prec \tau\}, \\ \mathcal{N}_\sigma^\uparrow &= \{\sigma' \mid \exists \tau \in \mathcal{C}_\sigma \text{ such that } \sigma, \sigma' \prec \tau\}, \end{aligned}$$

so that two simplices are upper-adjacent if they share a common coface. Simplex representations are updated according to

$$\mathbf{h}_\sigma^{t+1,(i)} = \phi \left(\mathbf{h}_\sigma^{t,(i)}, \text{AGG}_{\sigma' \in \mathcal{N}_\sigma^\uparrow} \psi \left(\mathbf{h}_\tau^{(i)}, \mathbf{h}_{\sigma'}^{t,(i)} \right) \right),$$

where τ is the shared coface of $\{\sigma, \sigma'\}$. The coface feature $\mathbf{h}_\tau^{(i)}$ contributes to the update of lower-dimensional simplices, analogous to generalized graph convolution operators [65]. Here, AGG is softmax aggregation, ψ is addition followed by ReLU, and ϕ is addition followed by an MLP.

Cross-scale refinement

Cross-scale refinement enriches finer-scale simplex representations using long-range interaction information (Figure 2(b)). Since any filtration is a nested sequence of subcomplexes, any simplex $\sigma \in \text{VR}_{\epsilon_i}$ also exists in $\text{VR}_{\epsilon_{i+1}}$, and we define its refined representation as

$$\mathbf{x}'_{\sigma, \epsilon_i} = \mathbf{x}_{\sigma, \epsilon_i} + \mathbf{x}_{\sigma, \epsilon_{i+1}} \odot \text{MLP} \left(\mathbf{x}_{\sigma, \epsilon_{i+1}} \parallel \text{MLP}(\mathbf{x}_{\sigma, \epsilon_{i+1}}) \right),$$

where the coarse-scale representation $\mathbf{x}_{\sigma, \epsilon_{i+1}}$ is used to produce a gated modulation vector via MLP, which is then added residually to the finer-scale features $\mathbf{x}_{\sigma, \epsilon_i}$ before the next round of multi-head message passing.

End-to-end pipeline

The HSMP encoder combines the above two simplex update functions into a systematic pipeline for learning polymer representations, with a schematic provided in Figure 2(c). Starting from a pSMILES representation, we computed a periodic distance matrix and applied a Vietoris–Rips filtration at three cutoff distances, $\epsilon_3 = 4.0 \text{ \AA}$, $\epsilon_2 = 3.0 \text{ \AA}$, and $\epsilon_1 = 2.0 \text{ \AA}$. Initial simplex features comprised atom and bond descriptors commonly used in molecular GNNs [28, 66], augmented with Forman’s discretization of Ricci curvature [44, 67–69] as a geometry-aware simplex feature applicable to any dimension [70–72]. Detailed feature descriptions and the formal definition of Forman curvature are provided in the Methods section and Supplementary Information.

Message passing proceeds hierarchically from the coarsest to the finest scale. At ϵ_3 , node and edge representations are updated via co-boundary and upper-adjacent relations, after which cross-scale refinement transfers information to ϵ_2 . This process repeats through to ϵ_1 , where message passing is restricted to the covalent bond graph. Here, atom and bond features are augmented by curvature descriptors from $\text{VR}_{\epsilon_1}(\mathbf{D})$. This architecture enforces hierarchy along two directions. Within each filtration level, information flows from higher-order to lower-order structures. Across levels, it flows in order of decreasing cutoff. Consequently, atom and bond representations at the covalent scale already incorporate geometry-enhanced signals from higher-dimensional simplices and coarser filtration levels.

Pretraining and fine-tuning

We pretrained HSMP using three self-supervised tasks adapted from the GROVER framework [56], namely atom context prediction, bond context prediction, and functional group (FG) prediction. The first two were formulated

as node and edge classification tasks, where the model predicted discrete context labels encoding local chemical environments from atom and bond features. FG prediction is a polymer-level multi-label classification task requiring a global representation, obtained via mean pooling over atom embeddings:

$$\mathbf{z}_{\text{polymer}} = \frac{1}{|\mathcal{V}|} \sum_{u \in \mathcal{V}} \mathbf{z}_u,$$

where \mathcal{V} denotes the set of atoms and \mathbf{z}_u are the learned atom embeddings at ϵ_1 . This pooling operation was also applied during fine-tuning for downstream polymer property prediction, where pretrained weights provide an informed initialization that transfers both local and global chemical context. The pretraining and fine-tuning pipelines are illustrated in Figure 2(d).

Periodic-TDL Outperforms Baselines Across Diverse Polymer Properties

We pretrained the HSMP encoder on the PIIM dataset of one million polymers [73] and finetuned it on nine downstream tasks spanning electronic (E_{gc} , E_{ib} [74], E_{gb} , E_{ea} , E_i [75]), optical (EPS, N_c [75]), physical (X_c [75]), and thermal (T_g [76]) properties. Here, T_g is experimentally measured and the remainder are DFT-derived. Performance was assessed via five-fold cross-validation and reported as RMSE and R^2 on test folds. Summary statistics of the nine datasets are provided in **Table S1** and **Figure S1**. Experimental settings are described in Methods. Baselines spanned fingerprint-based (Morgan NN [77]), sequence-based (polyBERT [17], TransPolymer [16]), graph-based (polyGNN [28], MolCLR (GCN), MolCLR (GIN) [22]), and multimodal (TransChem [31], MMPolymer [30]) architectures, all evaluated on identical data splits. Baseline implementation details are provided in Supplementary Information.

TABLE I. Test RMSE (mean \pm std) for Periodic-TDL and baseline models across nine downstream polymer property prediction tasks spanning electronic, optical, physical, and thermal targets. Lower values indicate better performance. All models are evaluated on identical data splits using five-fold cross-validation. Best and second-best results per target are highlighted in **bold** and underline, respectively.

Model	E_{gc} (eV)	E_{ib} (eV)	E_{gb} (eV)	E_{ea} (eV)	E_i (eV)	EPS	N_c	X_c (%)	T_g ($^{\circ}$ C)
Morgan (NN)	0.559 \pm 0.010	0.642 \pm 0.073	0.860 \pm 0.042	0.431 \pm 0.018	0.720 \pm 0.047	0.737 \pm 0.034	0.167 \pm 0.008	19.41 \pm 0.97	37.99 \pm 1.27
polyBERT	0.483 \pm 0.020	0.574 \pm 0.081	0.626 \pm 0.058	0.333 \pm 0.009	<u>0.443 \pm 0.066</u>	<u>0.626 \pm 0.048</u>	0.113 \pm 0.006	19.74 \pm 0.82	36.33 \pm 1.89
TransPolymer	0.462 \pm 0.032	0.589 \pm 0.080	0.609 \pm 0.067	0.340 \pm 0.042	0.454 \pm 0.068	0.650 \pm 0.032	0.117 \pm 0.014	<u>19.19 \pm 0.70</u>	35.81 \pm 2.17
polyGNN	0.524 \pm 0.040	0.577 \pm 0.059	0.597 \pm 0.041	<u>0.309 \pm 0.031</u>	0.584 \pm 0.144	0.631 \pm 0.112	<u>0.109 \pm 0.011</u>	21.23 \pm 1.45	43.35 \pm 0.74
MolCLR (GCN)	0.555 \pm 0.018	0.573 \pm 0.076	0.702 \pm 0.098	0.391 \pm 0.039	0.550 \pm 0.074	0.629 \pm 0.073	0.118 \pm 0.011	20.66 \pm 1.01	44.10 \pm 1.99
MolCLR (GIN)	0.484 \pm 0.022	0.549 \pm 0.067	0.627 \pm 0.078	0.341 \pm 0.029	0.564 \pm 0.126	0.641 \pm 0.065	0.121 \pm 0.010	20.77 \pm 1.32	41.53 \pm 1.08
TransChem	0.483 \pm 0.031	0.637 \pm 0.081	0.656 \pm 0.061	0.376 \pm 0.056	0.504 \pm 0.153	0.663 \pm 0.084	0.114 \pm 0.007	19.64 \pm 0.69	<u>35.72 \pm 1.39</u>
MMPolymer	<u>0.448 \pm 0.019</u>	0.606 \pm 0.053	<u>0.596 \pm 0.056</u>	0.342 \pm 0.028	0.493 \pm 0.089	0.691 \pm 0.059	0.120 \pm 0.015	19.33 \pm 1.59	35.77 \pm 1.98
Periodic-TDL	0.441 \pm 0.022	<u>0.554 \pm 0.084</u>	0.547 \pm 0.087	0.294 \pm 0.022	0.406 \pm 0.059	0.535 \pm 0.043	0.098 \pm 0.006	18.22 \pm 0.77	34.68 \pm 2.17

Periodic-TDL achieved the lowest RMSE on eight of nine tasks and the highest R^2 on all nine (**Tables I** and **S2** respectively), with consistent gains across all property types. No single baseline ranked consistently among the top performers across tasks. For eight of nine targets, mean RMSE of Periodic-TDL was 50–75% lower than the standard deviation of the dataset. Specifically, for the T_g dataset, RMSE was approximately 35 $^{\circ}$ C against a standard deviation of 110 $^{\circ}$ C (69% reduction). Normalized RMSE, as shown alongside parity plots in **Figure S2**, ranged from 4–7% for most targets, \sim 8% for EPS and \sim 20% for X_c . Ablation studies examining (i) the role of periodic representation and hierarchical message passing, and (ii) the effect of multi-head message passing, pretraining, and model capacity, suggest that performance degrades when any component is removed. A detailed summary of the ablation studies is provided in Supplementary Information, with results reported in **Tables S3**, **S4**, and **S5**.

Predicted T_g Trends in Acrylates and Acrylamides Are Chemically Credible

Next, we determined whether Periodic-TDL captures two trends in the glass transition temperature of acrylate- and acrylamide-based polymers, namely the effect of replacing ester with amide functional groups, and the effect of backbone α -methyl substitution. These trends are chosen because they are extensively documented in the experimental literature [78–85]. We evaluated chemical credibility in three steps. First, we analyzed predicted T_g distributions across

a dataset of 48208 systematically substituted vinyl polymers spanning four families. Second, we performed pairwise statistical analyses over 12052 matched polymer pairs to quantify the magnitude and consistency of predicted T_g shifts. Third, we compared these trends against experimentally measured T_g values from three independently synthesized polymers and eight polymers drawn from the experimental literature, all absent from the fine-tuning dataset.

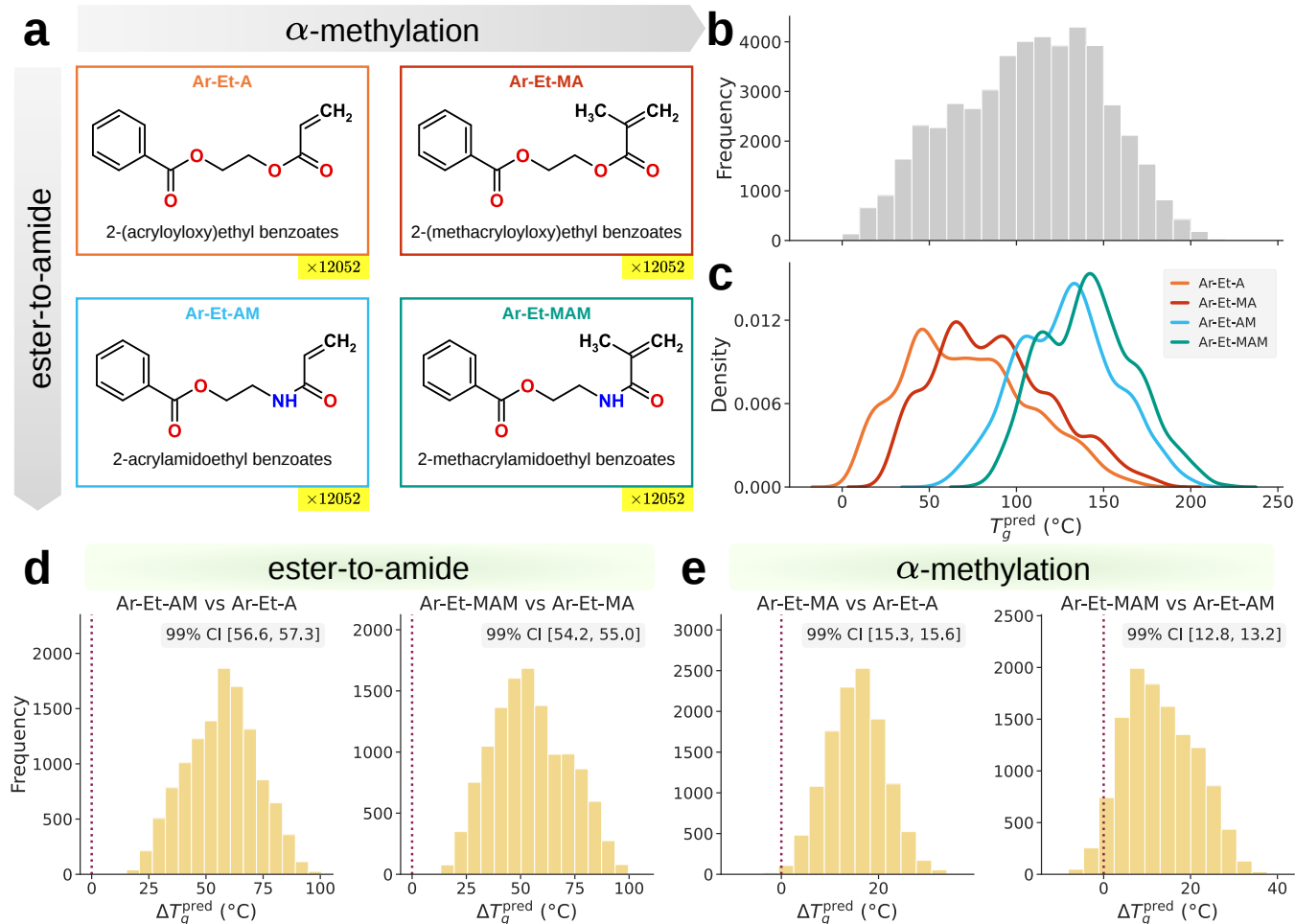


FIG. 3. Predicted glass transition temperature trends for systematically substituted acrylate- and acrylamide-based polymers. (a) Monomer structures for the four polymer families: poly(acrylate) (Ar-Et-A), poly(methacrylate) (Ar-Et-MA), poly(acrylamide) (Ar-Et-AM), and poly(methacrylamide) (Ar-Et-MAM), arranged to reflect the two structural modifications under study: ester-to-amide (vertical axis) and backbone α -methylation (horizontal axis). Systematic substitution on the phenyl ring yields 12,052 monomers per family. (b) Overall distribution of predicted T_g across the full dataset. (c) Stratified T_g distributions for each polymer family, showing systematic shifts associated with ester-to-amide substitution and α -methylation. (d) Distributions of pairwise ΔT_g^{pred} for matched polymer pairs differing by ester-to-amide substitution, with 99% confidence intervals. (e) Distributions of pairwise ΔT_g^{pred} for matched polymer pairs differing by α -methylation, with 99% confidence intervals.

Pendant Group Chemistry Drives Systematic T_g Shifts Across Polymer Families

We generated a computational dataset of 48208 monomer structures via systematic substitution on the phenyl ring of four monomers illustrated in Fig. 3(a). The dataset spans two ester-pendant families composed of substituted 2-(acryloyloxy)ethyl benzoates (Ar-Et-A) and 2-(methacryloyloxy)ethyl benzoates (Ar-Et-MA), and two amide-pendant families composed of substituted 2-acrylamidoethyl benzoates (Ar-Et-AM) and 2-methacrylamidoethyl benzoates (Ar-Et-MAM). Details of dataset generation are provided in Methods.

The overall distribution of predicted T_g across the full dataset spans approximately 0 °C to 225 °C, as shown in Fig. 3(b). When stratified by polymer family, distinct T_g distributions emerge for each of the four families [Fig. 3(c)],

with statistically significant differences confirmed across all comparisons ($p < 0.001$, see Methods). Mean T_g values for each family are reported in **Table S6**.

We further examined polymer candidates within low ($T_g^{\text{pred}} \leq 30^\circ\text{C}$), medium ($100^\circ\text{C} \leq T_g^{\text{pred}} \leq 130^\circ\text{C}$), and high ($T_g^{\text{pred}} \geq 200^\circ\text{C}$) predicted T_g ranges, yielding 1702, 12029, and 221 polymers, respectively. Schuffenhauer Synthetic Accessibility (SA) scores [86] computed for the corresponding monomers indicate that higher T_g ranges are associated with more synthetically challenging monomers (**Fig. S4**). This is consistent with bulkier, more polar, and hydrogen-bonding-capable pendant groups contributing to elevated T_g , as commonly observed in polymer chemistry.

Amide Substitution and α -Methylation Produce Consistent T_g Elevations

We evaluated the effect of ester-to-amide substitution and backbone α -methyl substitution on T_g^{pred} via pairwise analyses over 12052 matched monomer pairs, isolating each structural modification while controlling for all other aspects of monomer structure. Distributions of ΔT_g^{pred} for ester-to-amide and α -methylation comparisons are shown in Fig. 3(d) and Fig. 3(e) respectively, with 99% confidence intervals computed from the empirical distribution. Statistical analysis details are provided in Methods.

Replacing ester with amide pendant groups produced the largest and most consistent T_g elevation. The predicted shift was positive across all matched pairs for both the acrylate–acrylamide comparison (mean = 57.0°C , 99% CI: [56.6, 57.3]) and the methacrylate–methacrylamide comparison (mean = 54.6°C , 99% CI: [54.2, 55.0]). Backbone α -methyl substitution produced a smaller but statistically significant elevation in both the acrylate–methacrylate (mean = 15.4°C , 99% CI: [15.3, 15.6]) and the acrylamide–methacrylamide comparisons (mean = 13.0°C , 99% CI: [12.8, 13.2]), with a minority of matched pairs exhibiting negative ΔT_g^{pred} in both cases. All four comparisons were statistically significant ($p < 0.001$, two-sided t -test, corrected for multiple comparisons).

Predicted Directional Trends Are Confirmed by Experimental Measurements

To corroborate the trends identified above, we synthesized three polymers from the systematically created dataset, namely poly(2-(acryloyloxy)ethyl benzoate) (PBz-Et-A), poly(2-(methacryloyloxy)ethyl benzoate) (PBz-Et-MA), and poly(2-acrylamidoethyl benzoate) (PBz-Et-AM). All three polymers were absent from the fine-tuning dataset and have not been previously characterized in the experimental literature. Synthesis and characterization were carried out using identical experimental protocols, detailed in Supplementary Information. Table II reports predicted and experimentally measured T_g values for the three synthesized polymers. Two of the three predictions agree with experiment to within 4°C (PBz-Et-A and PBz-Et-MA), demonstrating that Periodic-TDL can achieve quantitative accuracy for novel polymers outside the fine-tuning dataset.

TABLE II. Experimental validation of predicted T_g for newly synthesized polymers. Three polymers absent from the fine-tuning dataset were synthesized and characterized using identical experimental protocols (see Supplementary Information). T_g^{exp} represents experimentally measured values. T_g^{pred} represents mean \pm SD across ten cross-validation folds as predicted by Periodic-TDL.

Abbrev.	Polymer	T_g^{exp} ($^\circ\text{C}$)	T_g^{pred} ($^\circ\text{C}$)
PBz-Et-A	poly(2-(acryloyloxy)ethyl benzoate)	7.3	7.4 ± 4.5
PBz-Et-MA	poly(2-(methacryloyloxy)ethyl benzoate)	32.7	29.1 ± 4.4
PBz-Et-AM	poly(2-acrylamidoethyl benzoate)	38.6	60.3 ± 5.7

For polymer design, directional accuracy across structurally related polymers is a crucial and practically relevant criterion, as it evaluates whether the model captures meaningful structure–property trends rather than only minimizing absolute errors in the training set. The three synthesized polymers yield two matched pairs, PBz-Et-A versus PBz-Et-AM (ester-to-amide effect) and PBz-Et-A versus PBz-Et-MA (α -methylation effect). To obtain a broader assessment spanning diverse pendant group chemistries, we supplement these with four additional polymer pairs drawn from the experimental literature, all absent from the fine-tuning dataset. Three pairs were selected preferentially from polymers bearing aromatic pendant groups, consistent with the chemical space of the systematically substituted dataset. One glycopolymer pair was also included to probe generalization to non-aromatic systems. Together, these yield six matched pairs covering both structural modifications under study. Table III reports predicted and experimental ΔT_g values for all six pairs. Predicted directional trends were in agreement with experiment in all six cases, spanning both ester-to-amide substitution and α -methylation effects across structurally diverse pendant group chemistries.

TABLE III. **Pairwise validation of predicted ΔT_g trends.** Six polymer pairs, each differing by a single structural modification (ester-to-amide substitution or backbone α -methylation), are evaluated for directional agreement between predicted and experimental ΔT_g values. Pairs marked as \dagger were synthesized in this work while remaining pairs were drawn from the experimental literature. All polymers were absent from the fine-tuning dataset. ΔT_g^{exp} denotes experimentally measured values. ΔT_g^{pred} denotes mean \pm SD across ten cross-validation folds. Directional agreement indicates whether the sign of ΔT_g^{pred} matches the sign of ΔT_g^{exp} . Full polymer names and individual T_g values are provided in Supplementary **Table S7**.

Modification	Polymer pair	ΔT_g^{exp} ($^{\circ}\text{C}$)	ΔT_g^{pred} ($^{\circ}\text{C}$)	Directional agreement
Ester-to-amide	PBz-Et-A \rightarrow PBz-Et-AM \dagger	31.3	52.9 ± 5.4	✓
Ester-to-amide	Poly-O \rightarrow Poly-A [78]	97.0	8.3 ± 5.3	✓
α -methylation	PBz-Et-A \rightarrow PBz-Et-MA \dagger	25.4	21.7 ± 3.3	✓
α -methylation	PSA \rightarrow PSMA [82]	10.0	11.1 ± 1.9	✓
α -methylation	PVA \rightarrow PVMA [82]	15.0	17.3 ± 3.1	✓
α -methylation	PGlc- β -EAAM \rightarrow PGlc- β -EMAAM [83]	23.5	4.2 ± 1.9	✓

Overall, the analyses presented here establish the chemical credibility of Periodic-TDL predictions. Ester-to-amide substitution and backbone α -methyl substitution each produce statistically significant T_g elevations across matched polymer pairs. The predicted directional trends are also confirmed against experimental measurements across pairs spanning diverse pendant group chemistries.

DISCUSSION

We introduce Periodic-TDL, a framework that encodes the periodic, many-body, and multiscale structure of polymers through a periodic Vietoris–Rips filtration. The Hierarchical Simplicial Message Passing (HSMP) encoder integrates information from higher-order simplices and long-range interactions into atom representations at the covalent scale. Pretrained on one million unlabelled polymers and finetuned on labelled datasets, Periodic-TDL achieves state-of-the-art performance across electronic, optical, physical, and thermal polymer properties. Beyond predictive accuracy, we assessed the chemical credibility of Periodic-TDL by examining the changes in T_g upon ester-to-amide substitution and backbone α -methylation in acrylate- and acrylamide-based polymers. Both effects have been noted as phenomenological observations and documented experimentally for isolated polymer pairs, but their magnitude and consistency across a systematically varied family of polymers have not previously been quantified. Periodic-TDL predicts that (meth)acrylamides exhibit higher T_g than (meth)acrylates, and methacrylates (methacrylamides) exhibit higher T_g than the corresponding acrylates (acrylamides). Specifically, ester-to-amide substitution produced a mean T_g elevation of $\sim 55,^{\circ}\text{C}$, while backbone α -methylation produced a smaller but statistically consistent elevation of $\sim 14,^{\circ}\text{C}$ across matched polymer pairs within our systematically substituted acrylate and acrylamide dataset. Both trends were further validated against experimental measurements from six polymer pairs, including three newly synthesized polymers absent from literature. Next, we discuss the mechanistic origins of these trends and speculate on how specific features of the Periodic-TDL architecture may account for its sensitivity to individual functional group modifications.

The T_g of polymers is influenced by the polarity, bulkiness, and flexibility of pendant groups. Specifically, the higher T_g of (meth)acrylamides relative to (meth)acrylates has been attributed to two mechanisms. First, the partial double-bond character of the C–N bond increases pendant-group stiffness in (meth)acrylamides, whereas the C–O bond in (meth)acrylates allows free rotation [78]. Second, the acrylamide group can act as both a hydrogen-bond donor and acceptor, enabling physical cross-linking between amide and carbonyl groups [79, 85]. The higher T_g of methacrylates (methacrylamides) relative to acrylates (acrylamides) has been attributed to steric hindrance from the α -methyl group, which restricts chain mobility [80, 82, 83]. The agreement with known trends likely arises from two features of Periodic-TDL. First, the periodic Vietoris–Rips filtration at larger cutoffs, $\epsilon_2 = 3.0 \text{ \AA}$ and $\epsilon_3 = 4.0 \text{ \AA}$, incorporates interactions at length scales relevant to non-covalent contacts such as hydrogen bonding. Second, the additional α -methyl group increases local steric density, leading to more higher-dimensional simplices at intermediate cutoffs. This structural difference is likely reflected in curvature-based simplex features, where more positive Forman–Ricci curvature indicates locally dense regions in the complex.

A distinctive feature of Periodic-TDL is its integration of multiscale interactions across filtration levels. Existing deep learning frameworks that incorporate filtration typically treat each cutoff independently and obtain a final molecular representation by pooling and concatenating features across cutoffs [55, 87, 88]. In contrast, the HSMP encoder processes all cutoffs within a unified hierarchical pipeline. Information propagates from coarser to finer spatial scales through cross-scale refinement, such that atom and bond representations at the covalent scale already incorporate contributions from higher-order simplices and long-range interactions. This design preserves compatibility with established graph-based pretraining workflows, allowing HSMP to replace conventional graph encoders without requiring new pretraining objectives. To our knowledge, this work is also the first to incorporate discrete curvature into a TDL framework. In particular, Forman–Ricci curvature provides a principled initial signal for simplices of any dimension, which is necessary for message passing to operate meaningfully on higher-order topological domains.

Several limitations of the current work point to promising future directions. First, Periodic-TDL is currently restricted to linear homopolymers and does not yet handle copolymers, for which additional information on stoichiometry and chain architecture would be required [25, 89]. Second, the periodic Vietoris–Rips complex is constructed from cyclic permutations of a single repeating unit and therefore does not explicitly encode interactions between atoms in distant repeat units. Quotient complex constructions have been successfully applied to crystalline materials with three-dimensional periodicity [90, 91]. However, many synthetic polymers are semicrystalline or amorphous rather than fully crystalline, and a careful assessment is therefore needed to determine whether such constructions can be transferred to polymer systems. Third, crosslinking is not represented in the current framework, despite being a structural factor that strongly influences T_g [92, 93]. Finally, our computational analysis suggests that higher- T_g polymers tend to be bulkier and more polar. This trend could be tested systematically through targeted synthesis of candidates selected across the predicted T_g range.

METHODS

Construction of the Periodic Vietoris–Rips Complex

We considered linear homopolymers composed of a single repeating unit arranged along an unbranched backbone. To construct a representation that was invariant to the arbitrary choice of the repeating unit, we generated all possible units following the fragmentation and rearrangement scheme proposed in Lo et al. [61]. Specifically, we first identified a backbone via the shortest path between the two terminal dummy atoms. Bonds along this backbone that were not part of rings were treated as breakable, yielding fragments that can be cyclically permuted while preserving chemical connectivity. Side-chain atoms remained attached to their corresponding backbone fragment. Each cyclic permutation produced a valid repeating unit with identical composition but shifted endpoints along the backbone. Connectivity was preserved across all permutations.

Let N be the number of atoms in the smallest unit and let the atom index set be $S = \{1, 2, \dots, N\}$. Let K denote the number of unique units generated using cyclic permutations. For each unique unit with index $k \in \{1, \dots, K\}$, let $e_\alpha^{(k)} \in \mathbb{R}^3$ denote the three-dimensional coordinate of atom α . The periodic distance matrix $\mathbf{D} \in \mathbb{R}_{\geq 0}^{N \times N}$ was defined as

$$\mathbf{D}_{\alpha\beta} = \min_k \|e_\alpha^{(k)} - e_\beta^{(k)}\|.$$

The above construction aggregates geometric information across all cyclic permutations and yields a distance matrix that is invariant to any particular choice of repeating unit. Given the periodic distance matrix \mathbf{D} , the Vietoris–Rips complex at scale $\epsilon_i > 0$ is defined as [41–43]

$$\text{VR}_{\epsilon_i}(\mathbf{D}) = \{\sigma \subseteq S \mid \mathbf{D}_{\alpha\beta} \leq \epsilon_i \quad \forall \alpha, \beta \in \sigma\}.$$

Thus, vertices correspond to atoms, edges correspond to atom pairs within distance ϵ , and higher-dimensional simplices encode multi-body interactions among atoms whose pairwise distances do not exceed ϵ_i .

For the Periodic-TDL framework, we chose a nested filtration of Vietoris–Rips complexes at increasing spatial scales

$$\text{VR}_{\epsilon_1}(\mathbf{D}) \subset \text{VR}_{\epsilon_2}(\mathbf{D}) \subset \text{VR}_{\epsilon_3}(\mathbf{D}).$$

Here, $\epsilon_1 = 2.0 \text{ \AA}$, $\epsilon_2 = 3.0 \text{ \AA}$, and $\epsilon_3 = 4.0 \text{ \AA}$. These cutoff values were fixed for all polymers used to train our model. The complex at $\epsilon_1 = 2 \text{ \AA}$ operates at the scale of covalent bonds, while ϵ_2 and ϵ_3 progressively incorporate non-covalent interactions [62]. The pseudocode of the procedure used to construct the periodic distance matrix, and formal backgrounds on simplicial complexes and Vietoris–Rips filtration are provided in **Supplementary Information**.

Initialization of Simplicial Features Across Filtration Levels

For each filtration level ϵ_i , we assigned vertex (0-simplex), edge (1-simplex), and triangle (2-simplex) features that combine chemical descriptors with curvature-based geometric information. Chemical descriptors were invariant across filtration levels since they only capture properties associated with covalent bonds. On the other hand, curvature features were computed independently for each ϵ_i , reflecting the scale-dependent topology induced by the cutoff parameter. For a vertex u , the initial feature vector was defined as

$$\mathbf{x}_{u,\epsilon_i} = [\mathbf{x}_u^{\text{atom}} \parallel \mathbf{x}_{u,\epsilon_i}^{\text{curv}}].$$

For an edge e ,

$$\mathbf{x}_{e,\epsilon_i} = [\mathbf{x}_e^{\text{bond}} \parallel \mathbf{x}_{e,\epsilon_i}^{\text{curv}}].$$

For a 2-simplex f , only geometric information was assigned via curvature features,

$$\mathbf{x}_{f,\epsilon_i} = \mathbf{x}_{f,\epsilon_i}^{\text{curv}}.$$

All simplex features were subsequently mapped to a common hidden dimension via learnable linear projections prior to multi-head simplicial message passing.

Chemical Features

Chemical descriptors were computed using RDKit [94]. These encode local atomic and covalent bond properties and depend only on the underlying molecular graph derived from the repeating unit. Each vertex u was assigned an atom-level feature vector $\mathbf{x}_u^{\text{atom}} \in \mathbb{R}^{70}$ constructed from one-hot encodings of atomic properties, including element type, atomic degree, implicit valence, formal charge, number of radical electrons, hybridization state, and aromaticity. For edges corresponding to covalent bonds, a bond-level descriptor $\mathbf{x}_e^{\text{bond}} \in \mathbb{R}^6$ was assigned, consisting of one-hot encodings of bond type along with binary indicators for conjugation and ring membership. If an edge in the Vietoris–Rips complex did not correspond to a covalent bond, its bond feature vector was set to the zero vector $\mathbf{x}_e^{\text{bond}} = \mathbf{0}$ in \mathbb{R}^6 . This served as an explicit masking mechanism indicating the absence of covalent bond attributes, while geometric information was retained through curvature-based features.

Curvature Features

Geometric features were derived from Forman’s discretization of curvature [44, 67–70], which assigns a curvature function on simplices of any dimension. Given a Vietoris–Rips complex $\text{VR}_{\epsilon_i}(\mathbf{D})$, curvature values were computed for vertices, edges, and triangles. We denote the curvature of a simplex σ at threshold ϵ_i by $\mathcal{F}_{\epsilon_i}(\sigma)$.

To incorporate geometric information from intermediate interaction scales without explicitly performing message passing at all thresholds, we calculated Forman curvature over a finer set of Vietoris–Rips complexes around each base cutoff ϵ_i . Specifically, for each ϵ_i , additional Vietoris–Rips complexes were generated at thresholds

$$\epsilon_i + k\Delta, \quad k = 0, 1, 2, 3, 4, \quad \Delta = 0.25 \text{ \AA}.$$

Forman curvature was then computed independently on each resulting complex. For example, at the covalent-scale cutoff $\epsilon_1 = 2.0 \text{ \AA}$, curvature was evaluated at $\{2.0, 2.25, 2.5, 2.75, 3.0\} \text{ \AA}$, yielding five curvature values per simplex.

The curvature-based feature vector for a simplex σ at filtration level ϵ_i was defined as

$$\mathbf{x}_{\sigma,\epsilon_i}^{\text{curv}} = [\mathcal{F}_{\epsilon_i}(\sigma), \mathcal{F}_{\epsilon_i+\Delta}(\sigma), \mathcal{F}_{\epsilon_i+2\Delta}(\sigma), \mathcal{F}_{\epsilon_i+3\Delta}(\sigma), \mathcal{F}_{\epsilon_i+4\Delta}(\sigma)] \in \mathbb{R}^5.$$

Since Forman curvature may vary substantially in magnitude across complexes of different sizes, curvature values were normalized using a temperature-scaled sigmoid transformation

$$f_T(x) = \frac{1}{1 + \exp(-x/T)}, \quad T = 10,$$

followed by centering to the interval $(-1, 1)$ via $2f_T(x) - 1$. This transformation preserves the sign of curvature which encodes meaningful geometric information. For example, negative curvature often indicates bottleneck regions, whereas positive curvature corresponds to locally dense regions [67, 70]. Moreover, it prevents excessively large curvature values from slowing convergence and compromising the numerical stability of gradient updates. Details on the computation of Forman curvature on simplicial complexes are provided in **Supplementary Information**.

Unlabelled and Labelled Polymer Datasets

The HSMP architecture in Periodic-TDL serves as a geometric encoder that maps a polymer to its latent space representation. To learn representations that are transferable across polymer property prediction tasks, we adopt a two-stage training protocol consisting of large-scale pretraining on an unlabelled dataset followed by supervised fine-tuning on labelled downstream datasets.

For pretraining, we used the PI1M dataset [73], a benchmark resource in polymer informatics comprising approximately one million polymers represented as pSMILES strings [17]. PI1M was constructed by training a generative model on polymers curated from the PolyInfo database and subsequently sampling ~ 1 M synthetic polymers, thereby providing broad chemical diversity for representation learning. Each entry in PI1M corresponds to a monomer repeating unit encoded in pSMILES format, where the symbol “*” denotes dummy atoms indicating polymerization sites. We finetuned the HSMP encoder on nine regression datasets corresponding to polymer property prediction tasks: E_{gc} (bandgap, chain) [74], E_{ib} (electron injection barrier) [74], E_{gb} (bandgap, bulk) [75], E_{ea} (electron affinity) [75], E_i (ionization energy) [75], EPS (dielectric constant) [75], N_c (refractive index) [75], X_c (crystallization tendency) [75], and T_g (glass transition temperature) [76]. These targets span thermal, electronic, optical, and physical property classes. Electronic (E_{gc} , E_{ib} , E_{gb} , E_{ea} , E_i), optical (EPS, N_c), and physical (X_c) properties were derived from density functional theory calculations, whereas T_g corresponds to experimentally measured values. For each task, the original dataset consists of pSMILES strings of monomer repeating units paired with scalar property values. Summary statistics, including the number of samples, mean, standard deviation, and empirical range for each dataset, are reported in **Table S1**.

Both the unlabelled and labelled datasets provide polymer structures in pSMILES format, whereas the HSMP encoder operates on a periodic Vietoris–Rips filtration derived from three-dimensional atomic coordinates. For each polymer, we therefore generated 3D coordinates using RDKit by embedding the monomer and performing geometry optimization with the Universal Force Field (UFF) [95]. For every pSMILES string, we generated all equivalent monomer representations using the cyclic rearrangement scheme described earlier (also see **Supplementary Information**), and constructed their corresponding UFF-optimized 3D atomic coordinates prior to computing the periodic distance matrix. Since Periodic-TDL is designed for linear homopolymers, we retained only polymers with exactly two dummy atoms (“*”) in their pSMILES representation. Polymers for which UFF optimization failed were excluded. The resulting polymers in each dataset were used for pretraining or for five-fold cross-validation during supervised fine-tuning.

HSMP Encoder Configuration

The HSMP encoder within the Periodic-TDL framework contains multi-head simplicial message passing modules. These modules were fixed with a hidden dimension of 768 and 12 message-passing heads. Message passing was performed hierarchically across filtration levels with 4 edge-update layers followed by 6 node-update layers at the coarsest level (ϵ_3), 4 edge-update layers followed by 6 node-update layers at the intermediate level (ϵ_2), and 6 node-update layers at the finest level (ϵ_1). At the finest filtration level, the encoder produced atom-level and bond-level representations. Further, a polymer-level representation was obtained via global mean pooling of atom representations.

Pretraining Details

Our pretraining task consists of three self-supervised tasks defined on the atom, bond, and polymer level representations respectively: atom context prediction, bond context prediction, and functional-group (FG) prediction. These objectives were adapted from the molecular pretraining approach introduced in GROVER [56] to operate on periodic Vietoris–Rips filtration of polymers. For atom and bond context prediction, each atom and bond was assigned a discrete context string encoding its 1-hop local chemical environment under the canonical scheme described in [56]. The context strings were treated as categorical labels. The resulting vocabularies contained 4,580 atom context classes and 6,775 bond context classes. For each polymer, a random subset of atoms and bonds were selected as prediction targets with sampling fractions $p_{\text{atom}} = 0.15$ and $p_{\text{bond}} = 0.15$. Polymer-level supervision was incorporated through FG prediction, where a fixed set of 85 functional groups were defined using RDKit fragment descriptors. Since multiple functional groups may be present within a single polymer, FG prediction was formulated as a multi-label classification task.

The overall pretraining objective was defined as a weighted sum of the three losses:

$$\mathcal{L}_{\text{total}} = w_{\text{atom}}\mathcal{L}_{\text{atom}} + w_{\text{bond}}\mathcal{L}_{\text{bond}} + w_{\text{fg}}\mathcal{L}_{\text{fg}},$$

where $\mathcal{L}_{\text{atom}}$ and $\mathcal{L}_{\text{bond}}$ are categorical cross-entropy losses, and \mathcal{L}_{fg} is binary cross-entropy. The loss weights were fixed to $w_{\text{atom}} = 2.0$, $w_{\text{bond}} = 1.0$, and $w_{\text{fg}} = 5.0$ in all experiments. During pretraining, 95% of the PIIM dataset was used for optimization and 5% was held out for validation. Models were optimized using AdamW [96] with learning rates of 2×10^{-4} for the encoder and 10^{-3} for the task-specific prediction heads. A weight decay of 10^{-4} was applied to all parameters, and gradients were clipped using a threshold of 5.0 [97]. No dropout was applied during pretraining. Training was performed for 10 epochs with a batch size of 64. Model checkpoints were saved after each epoch, and the final model was selected based on the lowest validation loss. The selected checkpoint achieved a training loss of 0.0763 and a validation loss of 0.0593.

Finetuning Details

As a final step of the Periodic-TDL framework, we finetuned the HSMP encoder on nine supervised polymer property prediction tasks. A regression head consisting of a two-layer multilayer perceptron was attached to the polymer-level representation obtained by global mean pooling of the learned atom embeddings. All models were trained using mean squared error (MSE) loss. Model performance was evaluated using root mean squared error (RMSE), and the coefficient of determination (R^2), with RMSE used exclusively for early stopping and checkpoint selection.

In the first stage of the fine-tuning process, the encoder was frozen and only the regression head was optimized [98] for 10 epochs using AdamW [96] with a learning rate of 1×10^{-3} . In the second stage, the encoder was unfrozen and both encoder and head parameters were jointly optimized for a total of 60 epochs. During the joint optimization, learning rates of 1×10^{-4} and 1×10^{-3} were used for the encoder and regression head, respectively. A cosine learning rate schedule with periodic restarts was applied throughout training [99]. Gradients were clipped using a threshold of 5.0 [97]. The final model was selected as the checkpoint achieving the lowest validation RMSE over the entire training trajectory. No target scaling was applied for any downstream task.

All experiments were conducted using predefined five-fold cross-validation splits that were shared across HSMP and all baseline models. For each fold, 80% of the data was used for training and 20% was held out for testing. From the training portion, 20% was further reserved as a validation set for early stopping and model selection [100]. The test split was never used for hyperparameter selection or checkpoint selection.

All property prediction tasks were performed with the same training schedule and learning rates described above. Weight decay, regression head dropout, and batch size were varied according to dataset size. Weight decay was set to 0.0 for T_g and E_{gc} , 0.05 for E_{ib} , and 0.02 for the remaining datasets. Regression head dropout was set to 0.0 for T_g , E_{gc} , and E_{ib} , and to 0.1 for E_{gb} , E_{ea} , E_i , EPS, N_c , and X_c . We chose batch sizes of 64 for T_g , E_{gc} , and E_{ib} ; 32 for E_{gb} ; and 24 for E_{ea} , E_i , EPS, N_c , and X_c . No automated hyperparameter tuning was performed. Hyperparameters were determined once based on dataset size and applied consistently across folds.

Systematically Substituted Polymer Dataset

We generated a comprehensive dataset of systematically substituted polymers to evaluate structure-property relationships in glass transition temperature. Four unsubstituted monomer scaffolds were selected as base structures: 2-(acryloyloxy)ethyl benzoate (Ar-Et-A), 2-(methacryloyloxy)ethyl benzoate (Ar-Et-MA), 2-acrylamidoethyl benzoate (Ar-Et-AM), and 2-methacrylamidoethyl benzoate (Ar-Et-MAM). These scaffolds represent the four backbone families poly(acrylate), poly(methacrylate), poly(acrylamide), and poly(methacrylamide), enabling direct comparison of ester versus amide functional groups and the presence versus absence of α -methyl substitution.

For each scaffold, systematic substitution was performed on the phenyl ring at the ortho, meta, and para positions. We considered four substitution patterns: (i) no substituent, (ii) mono-substitution, (iii) di-substitution, and (iv) tri-substitution. At each substituted position, we assigned one of thirteen functional groups including alkyl and halogens. All substituted monomer structures were generated and subsequently converted to pSMILES strings. This procedure yielded 12,052 unique monomers per family and 48,208 polymers total across the four families.

Glass Transition Temperature Prediction

To obtain predicted T_g values for the systematically substituted dataset, we applied considered the experimental T_g dataset used for benchmarking Periodic-TDL. Each polymer was converted to its periodic Vietoris-Rips complex representation and processed through the HSMP encoder. The training data was randomly divided into ten folds. For each fold, the HSMP encoder was trained on nine folds while the tenth fold was used for early stopping. This

yielded ten models optimized on disjoint validation splits. Importantly, none of the generated or validation polymers were used during training.

For inference on the generated dataset, literature polymers, and newly synthesized polymers, each polymer pSMILES was processed through the HSMP encoder using all ten trained models. The predicted T_g for each polymer was obtained by averaging the outputs from the ten models, with uncertainty quantified as the standard deviation across the ensemble. Predicted values are reported as mean \pm standard deviation.

Statistical Analysis of Predicted Glass Transition Temperatures

Family-wise T_g distributions were characterized by computing mean and standard deviation for each of the four polymer families (Ar–Et–A, Ar–Et–MA, Ar–Et–AM, Ar–Et–MAM). To test for significant differences between families, we applied two-sample Mann–Whitney U tests to each pair of families using a two-sided alternative hypothesis. The resulting p-values were corrected using the Holm method to control the family-wise error rate, and differences with corrected $p < 0.001$ were considered statistically significant.

To isolate the effects of specific structural modifications, we constructed matched polymer pairs across families using the recorded ring-substitution patterns and substituent identities. Four pairwise comparisons were performed: (i) Ar–Et–AM versus Ar–Et–A (ester-to-amide), (ii) Ar–Et–MAM versus Ar–Et–MA (ester-to-amide), (iii) Ar–Et–MA versus Ar–Et–A (α -methylation), and (iv) Ar–Et–MAM versus Ar–Et–AM (α -methylation). We tested whether mean ΔT_g deviated significantly from zero using two-sided one-sample t -tests. Confidence intervals (99%) were calculated from the t -distribution.

Literature Validation, Experimental Synthesis and Characterization

To validate predicted trends against experimental observations, we identified published reports describing the effect of replacing ester with amide functional groups or adding α -methyl substitution in acrylic polymers. We selected studies with matched structures consistent with our computational analyses and reliable experimental T_g values. This yielded 8 polymers comprising 4 matched pairs. For each literature polymer, the monomer structure was converted to a pSMILES string and the predicted T_g was obtained using the ensemble procedure described above. Polymers were grouped into pairs matching the literature structural modifications, and we computed $\Delta T_g^{(\text{pred})}$ and $\Delta T_g^{(\text{lit})}$ for each pair. Directional agreement was assessed by determining whether the predicted and experimental ΔT_g values shared the same sign.

To provide independent experimental validation, we synthesized three polymers that were entirely absent from the training dataset and had not been previously characterized in the experimental literature, namely poly(2-(acryloyloxy)ethyl benzoate), poly(2-(methacryloyloxy)ethyl benzoate), and poly(2-acrylamidoethyl benzoate). These polymers were selected to enable direct evaluation of both ester-to-amide and α -methylation effects. Detailed synthesis and characterization conditions are provided in the Supplementary Information. Predicted T_g values were compared with experimental measurements to assess model accuracy on independently synthesized materials.

To assess the feasibility of synthesizing the generated polymer library, we computed Schuffenhauer Synthetic Accessibility (SA) scores for all 48,208 monomers. SA scores range from 1 (highly synthesizable) to 10 (very difficult to synthesize). Polymers were categorized into three T_g ranges: low ($T_g \leq 30^\circ\text{C}$), medium ($100^\circ\text{C} \leq T_g \leq 130^\circ\text{C}$), and high ($T_g \geq 200^\circ\text{C}$). For each range, we examined the distribution of SA scores and identified monomers with the lowest SA scores as promising synthetic targets.

DATA AVAILABILITY

The pretraining dataset (PI1M [73]) and the downstream fine-tuning datasets [74–76] used in this work are made available in their respective original publications. All datasets are also deposited in our GitHub repository at <https://github.com/yasharthy/Periodic-TDL>. The systematically substituted polymer dataset of 48208 structures, together with predicted T_g values across all ten cross-validation folds, and the experimental characterization data for the three independently synthesized polymers, together with their corresponding predicted T_g values, are deposited in the same repository.

CODE AVAILABILITY

All code for the construction of the periodic Vietoris–Rips complex, the Hierarchical Simplicial Message Passing (HSMP) encoder, and the pretraining and fine-tuning pipelines is publicly available at <https://github.com/yasharthy/Periodic-TDL>.

ACKNOWLEDGMENTS

This work was supported in part by the Singapore Ministry of Education Academic Research fund Tier 1 grant RG16/23, Tier 2 grants MOE-T2EP20125-0004 and MOE-T2EP50223-0036. The computational work for this article was partially performed on resources of the National Supercomputing Centre (NSCC), Singapore (<https://www.nsc.sg>).

AUTHOR CONTRIBUTIONS

K.X. conceived and designed the research. Y.Y. performed the computational work and simulations. T.K.G.E. conducted the experiments. All authors contributed to writing and revising the manuscript.

COMPETING INTERESTS

There are no competing interests to declare.

-
- [1] Roland Geyer, Jenna R Jambeck, and Kara Lavender Law. Production, use, and fate of all plastics ever made. *Science advances*, 3(7):e1700782, 2017.
 - [2] Jeffrey Lopez, David G Mackanic, Yi Cui, and Zhenan Bao. Designing polymers for advanced battery chemistries. *Nature Reviews Materials*, 4(5):312–330, 2019.
 - [3] Thomas Leigh and Paco Fernandez-Trillo. Helical polymers for biological and medical applications. *Nature Reviews Chemistry*, 4(6):291–310, 2020.
 - [4] Norman Gerard McCrum, C Paul Buckley, and Clive B Bucknall. *Principles of polymer engineering*. Oxford University Press, 1997.
 - [5] Michael M Coleman. *Fundamentals of polymer science: An introductory text*. Routledge, 2019.
 - [6] Dorel Feldman. Polymer history. *Designed monomers and polymers*, 11(1):1–15, 2008.
 - [7] Debra J Audus and Juan J de Pablo. Polymer informatics: opportunities and challenges. *ACS macro letters*, 6(10):1078–1082, 2017.
 - [8] Lihua Chen, Ghanshyam Pilania, Rohit Batra, Tran Doan Huan, Chiho Kim, Christopher Kuenneth, and Rampi Ramprasad. Polymer informatics: Current status and critical next steps. *Materials Science and Engineering: R: Reports*, 144:100595, 2021.
 - [9] Stephen Wu, Yukiko Kondo, Masa-aki Kakimoto, Bin Yang, Hironao Yamada, Isao Kuwajima, Guillaume Lambard, Kenta Hongo, Yibin Xu, Junichiro Shiomi, et al. Machine-learning-assisted discovery of polymers with high thermal conductivity using a molecular design algorithm. *Npj Computational Materials*, 5(1):66, 2019.
 - [10] J Wesley Barnett, Connor R Bilchak, Yiwen Wang, Brian C Benicewicz, Laura A Murdock, Tristan Bereau, and Sanat K Kumar. Designing exceptional gas-separation polymer membranes using machine learning. *Science advances*, 6(20):eaaz4301, 2020.
 - [11] Christopher Kuenneth, Jessica Lalonde, Babetta L Marrone, Carl N Iverson, Rampi Ramprasad, and Ghanshyam Pilania. Bioplastic design using multitask deep neural networks. *Communications materials*, 3(1):96, 2022.
 - [12] David Rogers and Mathew Hahn. Extended-connectivity fingerprints. *Journal of chemical information and modeling*, 50(5):742–754, 2010.
 - [13] Chiho Kim, Anand Chandrasekaran, Tran Doan Huan, Deya Das, and Rampi Ramprasad. Polymer genome: a data-powered polymer informatics platform for property predictions. *The Journal of Physical Chemistry C*, 122(31):17575–17585, 2018.
 - [14] Huan Doan Tran, Chiho Kim, Lihua Chen, Anand Chandrasekaran, Rohit Batra, Shruti Venkatram, Deepak Kamal, Jordan P Lightstone, Rishi Gurnani, Pranav Shetty, et al. Machine-learning predictions of polymer properties with polymer genome. *Journal of Applied Physics*, 128(17), 2020.

- [15] Simon Axelrod, Daniel Schwalbe-Koda, Somesh Mohapatra, James Damewood, Kevin P Greenman, and Rafael Gómez-Bombarelli. Learning matter: Materials design with machine learning and atomistic simulations. *Accounts of Materials Research*, 3(3):343–357, 2022.
- [16] Changwen Xu, Yuyang Wang, and Amir Barati Farimani. TransPolymer: a Transformer-based language model for polymer property predictions. *npj Computational Materials*, 9(1):64, 2023.
- [17] Christopher Kuenneth and Rampi Ramprasad. polyBERT: a chemical language model to enable fully machine-driven ultrafast polymer informatics. *Nature Communications*, 14(1):4099, 2023.
- [18] Sandhya Alagarsamy, Chin-Shiuh Shieh, Mong-Fong Horng, Subhashini Radhakrishnan, Sethuraman Radhakrishnan, and Abdelwahab Omri. Transformers in drug discovery: fine-tuning chemberta for high-accuracy prediction of solubility, toxicity and binding affinity. *Drug Discovery Today*, page 104602, 2026.
- [19] David Weininger. Smiles, a chemical language and information system. 1. introduction to methodology and encoding rules. *Journal of chemical information and computer sciences*, 28(1):31–36, 1988.
- [20] Chi Chen, Weiye Ye, Yunxing Zuo, Chen Zheng, and Shyue Ping Ong. Graph networks as a universal machine learning framework for molecules and crystals. *Chemistry of Materials*, 31(9):3564–3572, 2019.
- [21] Peter C St John, Caleb Phillips, Travis W Kemper, A Nolan Wilson, Yanfei Guan, Michael F Crowley, Mark R Nimlos, and Ross E Larsen. Message-passing neural networks for high-throughput polymer screening. *The Journal of chemical physics*, 150(23), 2019.
- [22] Yuyang Wang, Jianren Wang, Zhonglin Cao, and Amir Barati Farimani. Molecular contrastive learning of representations via graph neural networks. *Nature Machine Intelligence*, 4(3):279–287, 2022.
- [23] Somesh Mohapatra, Joyce An, and Rafael Gómez-Bombarelli. Chemistry-informed macromolecule graph representation for similarity computation, unsupervised and supervised learning. *Machine Learning: Science and Technology*, 3(1):015028, 2022.
- [24] Evan R. Antoniuk, Peggy Li, Bhavya Kailkhura, and Anna M. Hiszpanski. Representing Polymers as Periodic Graphs with Learned Descriptors for Accurate Polymer Property Predictions. *Journal of Chemical Information and Modeling*, 62(22):5435–5445, 2022.
- [25] Matteo Aldeghi and Connor W. Coley. A graph representation of molecular ensembles for polymer property prediction. *Chemical Science*, 13(35):10486–10498, 2022.
- [26] Esther Heid, Kevin P Greenman, Yunsie Chung, Shih-Cheng Li, David E Graff, Florence H Vermeire, Haoyang Wu, William H Green, and Charles J McGill. Chemprop: a machine learning package for chemical property prediction. *Journal of chemical information and modeling*, 64(1):9–17, 2023.
- [27] Owen Queen, Gavin A. McCarver, Saitheeraj Thatigotla, Brendan P. Abolins, Cameron L. Brown, Vasileios Maroulas, and Konstantinos D. Vogiatzis. Polymer graph neural networks for multitask property learning. *npj Computational Materials*, 9(1):90, 2023.
- [28] Rishi Gurnani, Christopher Kuenneth, Aubrey Toland, and Rampi Ramprasad. Polymer Informatics at Scale with Multitask Graph Neural Networks. *Chemistry of Materials*, 35(4):1560–1567, 2023.
- [29] Haoke Qiu, Lunyang Liu, Xuepeng Qiu, Xuemin Dai, Xiangling Ji, and Zhao-Yan Sun. Polync: a natural and chemical language model for the prediction of unified polymer properties. *Chemical Science*, 15(2):534–544, 2024.
- [30] Fanmeng Wang, Wentao Guo, Minjie Cheng, Shen Yuan, Hongteng Xu, and Zhifeng Gao. MMPolymer: A Multimodal Multitask Pretraining Framework for Polymer Property Prediction. In *Proceedings of the 33rd ACM International Conference on Information and Knowledge Management, CIKM '24*, pages 2336–2346. Association for Computing Machinery, 2024.
- [31] Vijith Parambil, Hritik Goyal, Ujjwal Tripathi, and Rohit Batra. TransChem: A hybrid transformer and cheminformatics based framework for enhanced polymer informatics. *Materials Today Communications*, 48:113375, 2025.
- [32] Qi Huang, Yedi Li, Lei Zhu, Qibin Zhao, and Wenjie Yu. Unified multimodal multidomain polymer representation for property prediction. *npj Computational Materials*, 11(1):153, 2025.
- [33] Liang Gao, Jiaping Lin, Liquan Wang, and Lei Du. Machine learning-assisted design of advanced polymeric materials. *Accounts of Materials Research*, 5(5):571–584, 2024.
- [34] Liang Gao, Siqin Song, Jiaping Lin, Yinyi Xu, Liquan Wang, and Lei Du. Ai-assisted design of advanced polymeric materials: Challenges and solutions. *Advanced Materials*, 38(7):e16857, 2026.
- [35] Gang Liu, Sobin Alosious, Subhamoy Mahajan, Eric Inae, Yihan Zhu, Yuhan Liu, Renzheng Zhang, Jiabin Xu, Addison Howard, Ying Li, et al. Open polymer challenge: Post-competition report. *arXiv preprint arXiv:2512.08896*, 2025.
- [36] Yoshihiro Yamauchi, Noriko Nishizawa Horimoto, Kuniyo Yamada, Yoshitaka Matsushita, Masayuki Takeuchi, and Yasuhiro Ishida. Two-step divergent synthesis of monodisperse and ultra-long bottlebrush polymers from an easily purifiable romp monomer. *Angewandte Chemie*, 133(3):1552–1558, 2021.
- [37] Mustafa Hajij, Ghada Zamzmi, Theodore Papamarkou, Nina Miolane, Aldo Guzmán-Sáenz, Karthikeyan Natesan Ramamurthy, Tolga Birdal, Tamal K Dey, Soham Mukherjee, Shreyas N Samaga, et al. Topological deep learning: Going beyond graph data. *arXiv preprint arXiv:2206.00606*, 2022.
- [38] Mustafa Hajij, Ghada Zamzmi, Theodore Papamarkou, Aldo Guzman-Saenz, ToIga Birdal, and Michael T Schaub. Combinatorial complexes: bridging the gap between cell complexes and hypergraphs. In *2023 57th Asilomar Conference on Signals, Systems, and Computers*, pages 799–803. IEEE, 2023.
- [39] Theodore Papamarkou, Tolga Birdal, Michael Bronstein, Gunnar Carlsson, Justin Curry, Yue Gao, Mustafa Hajij, Roland Kwitt, Pietro Lio, Paolo Di Lorenzo, et al. Position: Topological deep learning is the new frontier for relational learning. *Proceedings of machine learning research*, 235:39529, 2024.

- [40] Phu Pham, Quang-Thinh Bui, Ngoc Thanh Nguyen, Robert Kozma, Philip S Yu, and Bay Vo. Topological data analysis in graph neural networks: Surveys and perspectives. *IEEE Transactions on Neural Networks and Learning Systems*, 36(6):9758–9776, 2025.
- [41] Gunnar Carlsson. Topology and data. *Bulletin of the American Mathematical Society*, 46(2):255–308, 2009.
- [42] H. Edelsbrunner and J. Harer. *Computational Topology: An Introduction*. Applied Mathematics. American Mathematical Society, 2010.
- [43] Nina Otter, Mason A. Porter, Ulrike Tillmann, Peter Grindrod, and Heather A. Harrington. A roadmap for the computation of persistent homology. *EPJ Data Science*, 6(1):17, 2017.
- [44] Forman. Bochner’s Method for Cell Complexes and Combinatorial Ricci Curvature. *Discrete & Computational Geometry*, 29(3):323–374, 2003.
- [45] Jakob Hansen and Robert Ghrist. Toward a spectral theory of cellular sheaves. *Journal of Applied and Computational Topology*, 3(4):315–358, 2019.
- [46] Christian Bick, Elizabeth Gross, Heather A Harrington, and Michael T Schaub. What are higher-order networks? *SIAM review*, 65(3):686–731, 2023.
- [47] Cristian Bodnar, Fabrizio Frasca, Yuguang Wang, Nina Otter, Guido F. Montufar, Pietro Lió, and Michael Bronstein. Weisfeiler and Lehman Go Topological: Message Passing Simplicial Networks. In *Proceedings of the 38th International Conference on Machine Learning*, pages 1026–1037. PMLR, 2021.
- [48] Cristian Bodnar, Fabrizio Frasca, Nina Otter, Yuguang Wang, Pietro Lio, Guido F Montufar, and Michael Bronstein. Weisfeiler and lehman go cellular: Cw networks. *Advances in neural information processing systems*, 34:2625–2640, 2021.
- [49] Michael T Schaub, Jean-Baptiste Seby, Florian Frantzen, T Mitchell Roddenberry, Yu Zhu, and Santiago Segarra. Signal processing on simplicial complexes. In *Higher-order systems*, pages 301–328. Springer, 2022.
- [50] Lorenzo Giusti, Claudio Battiloro, Lucia Testa, Paolo Di Lorenzo, Stefania Sardellitti, and Sergio Barbarossa. Cell attention networks. In *2023 International Joint Conference on Neural Networks (IJCNN)*, pages 1–8. IEEE, 2023.
- [51] Zixuan Cang and Guo-Wei Wei. Topologynet: Topology based deep convolutional and multi-task neural networks for biomolecular property predictions. *PLoS computational biology*, 13(7):e1005690, 2017.
- [52] JunJie Wee and Jian Jiang. A review of topological data analysis and topological deep learning in molecular sciences. *Journal of Chemical Information and Modeling*, 65(23):12691–12706, 2025.
- [53] Lorenzo Giusti, Teodora Reu, Francesco Ceccarelli, Cristian Bodnar, and Pietro Lió. Topological message passing for higher-order and long-range interactions. In *2024 International Joint Conference on Neural Networks (IJCNN)*, pages 1–8. IEEE, 2024.
- [54] Amarjeet, Anurag Sinha, Khalid Hussain, Wasim Ahmad Bhat, Sudhanshu Maurya, Mohammad Nadeem Ahmed, Mohammad Rashid Hussain, and S Khalid. Topological graph neural networks: A novel approach for geometric deep learning. *Applied AI Letters*, 7(2):e70021, 2026.
- [55] Cong Shen, Yipeng Zhang, Tze Kwang Gerald Er, Fei Han, Atsushi Goto, and Kelin Xia. Molecular topological deep learning for polymer property prediction. *ACS nano*, 2026.
- [56] Yu Rong, Yatao Bian, Tingyang Xu, Weiyang Xie, Ying WEI, Wenbing Huang, and Junzhou Huang. Self-Supervised Graph Transformer on Large-Scale Molecular Data. In *Advances in Neural Information Processing Systems*, volume 33, pages 12559–12571. Curran Associates, Inc., 2020.
- [57] Xuan Zang, Xianbing Zhao, and Buzhou Tang. Hierarchical molecular graph self-supervised learning for property prediction. *Communications Chemistry*, 6(1):34, 2023.
- [58] Hanchen Wang, Jean Kaddour, Shengchao Liu, Jian Tang, Joan Lasenby, and Qi Liu. Evaluating self-supervised learning for molecular graph embeddings. *Advances in Neural Information Processing Systems*, 36:68028–68060, 2023.
- [59] Zaixi Zhang, Qi Liu, Hao Wang, Chengqiang Lu, and Chee-Kong Lee. Motif-based graph self-supervised learning for molecular property prediction. *Advances in Neural Information Processing Systems*, 34:15870–15882, 2021.
- [60] Bonyou Koo and Sunyoung Kwon. Comprehensive analysis of masking techniques in molecular graph representation learning. *IEEE Access*, 2025.
- [61] Stanley Lo, Martin Seifrid, Théophile Gaudin, and Alán Aspuru-Guzik. Augmenting Polymer Datasets by Iterative Rearrangement. *Journal of Chemical Information and Modeling*, 63(14):4266–4276, 2023.
- [62] Zixuan Cang, Lin Mu, and Guo-Wei Wei. Representability of algebraic topology for biomolecules in machine learning based scoring and virtual screening. *PLOS Computational Biology*, 14(1):e1005929, 2018.
- [63] Christopher Wei Jin Goh, Cristian Bodnar, and Pietro Lio. Simplicial attention networks. In *ICLR 2022 Workshop on Geometrical and Topological Representation Learning*, 2022.
- [64] Maosheng Yang, Elvin Isufi, and Geert Leus. Simplicial Convolutional Neural Networks. In *ICASSP 2022 - 2022 IEEE International Conference on Acoustics, Speech and Signal Processing (ICASSP)*, pages 8847–8851. IEEE, 2022.
- [65] Guohao Li, Chenxin Xiong, Ali Thabet, and Bernard Ghanem. DeeperGCN: All You Need to Train Deeper GCNs, 2020.
- [66] Jan G. Rittig, Qinghe Gao, Manuel Dahmen, Alexander Mitsos, and Artur M. Schweidtmann. Graph Neural Networks for the Prediction of Molecular Structure–Property Relationships. In *Machine Learning and Hybrid Modelling for Reaction Engineering: Theory and Applications*. Royal Society of Chemistry, 2023.
- [67] Areejit Samal, R. P. Sreejith, Jiao Gu, Shiping Liu, Emil Saucan, and Jürgen Jost. Comparative analysis of two discretizations of Ricci curvature for complex networks. *Scientific Reports*, 8(1):8650, 2018.
- [68] R. P. Sreejith, Karthikeyan Mohanraj, Jürgen Jost, Emil Saucan, and Areejit Samal. Forman curvature for complex networks. *Journal of Statistical Mechanics: Theory and Experiment*, 2016(6):063206, 2016.
- [69] R. P. Sreejith, Jürgen Jost, Emil Saucan, and Areejit Samal. Systematic evaluation of a new combinatorial curvature for complex networks. *Chaos, Solitons & Fractals*, 101:50–67, 2017.

- [70] JunJie Wee and Kelin Xia. Forman persistent ricci curvature (fprc)-based machine learning models for protein–ligand binding affinity prediction. *Briefings in Bioinformatics*, 22(6):bbab136, 2021.
- [71] Xin Lai, Yang Liu, Rui Qian, Yong Lin, and Qiwei Ye. Deeper Exploiting Graph Structure Information by Discrete Ricci Curvature in a Graph Transformer. *Entropy*, 25(6):885, 2023.
- [72] Lukas Fesser and Melanie Weber. Effective structural encodings via local curvature profiles. In *The Twelfth International Conference on Learning Representations*, 2024.
- [73] Ruimin Ma and Tengfei Luo. PI1M: A Benchmark Database for Polymer Informatics. *Journal of Chemical Information and Modeling*, 60(10):4684–4690, 2020.
- [74] Deepak Kamal, Huan Tran, Chiho Kim, Yifei Wang, Lihua Chen, Yang Cao, V. Roshan Joseph, and Rampi Ramprasad. Novel high voltage polymer insulators using computational and data-driven techniques. *The Journal of Chemical Physics*, 154(17):174906, 2021.
- [75] Christopher Kuenneth, Arunkumar Chitteth Rajan, Huan Tran, Lihua Chen, Chiho Kim, and Rampi Ramprasad. Polymer informatics with multi-task learning. *Patterns*, 2(4):100238, 2021.
- [76] Ivan Pavlovich Malashin, Vadim Sergeevich Tynchenko, Vladimir Aleksandrovich Nelyub, Aleksei Sergeevich Borodulin, and Andrei Pavlovich Gantimurov. Estimation and Prediction of the Polymers’ Physical Characteristics Using the Machine Learning Models. *Polymers*, 16(1):115, 2024. Number: 1.
- [77] H. L. Morgan. The Generation of a Unique Machine Description for Chemical Structures-A Technique Developed at Chemical Abstracts Service. *Journal of Chemical Documentation*, 5(2):107–113, 1965.
- [78] Alberto Gallardo and Julio San Roman. Effect of large polar side groups on the glass transition temperature of acrylic copolymers. *Macromolecules*, 26(14):3681–3686, 1993.
- [79] Elif Aydogan Ayaz and Rukiye Durkan. Influence of acrylamide monomer addition to the acrylic denture-base resins on mechanical and physical properties. *International Journal of Oral Science*, 5(4):229–235, 2013.
- [80] Friederike Fleischhaker, Alexander P. Haehnel, Andrea M. Misske, Mathieu Blanchot, Sylke Haremza, and Christopher Barner-Kowollik. Glass-Transition-, Melting-, and Decomposition Temperatures of Tailored Polyacrylates and Polymethacrylates: General Trends and Structure–Property Relationships. *Macromolecular Chemistry and Physics*, 215(12):1192–1200, 2014.
- [81] Leire Ruiz-Rubio, Verónica Álvarez, Erlantz Lizundia, José Luis Vilas, Matilde Rodríguez, and Luis Manuel León. Influence of α -methyl substitutions on interpolymer complexes formation between poly(meth)acrylic acids and poly(N-isopropyl(meth)acrylamide)s. *Colloid and Polymer Science*, 293(5):1447–1455, 2015.
- [82] Jinyong Zhou, Huanyu Zhang, Jianping Deng, and Youping Wu. High Glass-Transition Temperature Acrylate Polymers Derived from Biomasses, Syringaldehyde, and Vanillin. *Macromolecular Chemistry and Physics*, 217(21):2402–2408, 2016.
- [83] Azis Adharis, Dennis Vesper, Nick Koning, and Katja Loos. Synthesis of (meth)acrylamide-based glycomonomers using renewable resources and their polymerization in aqueous systems. *Green Chemistry*, 20(2):476–484, 2018.
- [84] Ying-Chieh Chuang, Kang-Ting Huang, Jin-Jia Hu, and Chun-Jen Huang. Mechanical and interfacial properties of zwitterionic hydrogels *via* a high-entanglement network design: a study of monomer and crosslinker synergy. *RSC Applied Polymers*, page 10.1039.D6LP00019C, 2026.
- [85] Cheng-Zhen Yuan, Yi-Chen Ou, Yu-Jui Pan, Shao-An Hua, and Hsiu-Wen Chien. Multifunctional poly(sulfobetaine acrylamide) hydrogel integrating robust mechanical properties, pH-triggered multicolor fluorescence, and antibacterial efficacy. *Dyes and Pigments*, 245:113177, 2026.
- [86] Peter Ertl and Ansgar Schuffenhauer. Estimation of synthetic accessibility score of drug-like molecules based on molecular complexity and fragment contributions. *Journal of Cheminformatics*, 1(1):8, 2009.
- [87] Cong Shen, Jiawei Luo, and Kelin Xia. Molecular geometric deep learning. *Cell reports methods*, 3(11), 2023.
- [88] Long D Nguyen, Kelin Xia, and Binh P Nguyen. Topology-aware multiscale mixture of experts for efficient molecular property prediction. *arXiv preprint arXiv:2601.12637*, 2026.
- [89] Tzyy-Shyang Lin, Connor W Coley, Hidenobu Mochigase, Haley K Beech, Wencong Wang, Zi Wang, Eliot Woods, Stephen L Craig, Jeremiah A Johnson, Julia A Kalow, et al. Bigsmiles: a structurally-based line notation for describing macromolecules. *ACS central science*, 5(9):1523–1531, 2019.
- [90] Chuan-Shen Hu, Rishikanta Mayengbam, Kelin Xia, and Tze Chien Sum. Quotient complex (qc)-based machine learning for 2d hybrid perovskite design. *Journal of Chemical Information and Modeling*, 65(2):660–671, 2025.
- [91] Xinyu You, Xiang Liu, Chuan-Shen Hu, Kelin Xia, and Tze Chien Sum. Quotient-complex transformer for perovskite data analysis. *Cell Reports Physical Science*, 2026.
- [92] Lawrence E Nielsen. Cross-linking–effect on physical properties of polymers. *Journal of Macromolecular Science, Part C*, 3(1):69–103, 1969.
- [93] Shintaro Nakagawa and Naoko Yoshie. Star polymer networks: a toolbox for cross-linked polymers with controlled structure. *Polymer Chemistry*, 13(15):2074–2107, 2022.
- [94] RDKit: Open-source cheminformatics <https://www.rdkit.org>.
- [95] A. K. Rappe, C. J. Casewit, K. S. Colwell, W. A. III Goddard, and W. M. Skiff. UFF, a full periodic table force field for molecular mechanics and molecular dynamics simulations. *Journal of the American Chemical Society*, 114(25):10024–10035, 1992.
- [96] Ilya Loshchilov and Frank Hutter. Decoupled Weight Decay Regularization. In *International Conference on Learning Representations*, 2019.
- [97] Razvan Pascanu, Tomas Mikolov, and Yoshua Bengio. On the difficulty of training recurrent neural networks. In *Proceedings of the 30th International Conference on Machine Learning*, volume 28, pages 1310–1318, Atlanta, Georgia,

USA, 2013. PMLR.

- [98] Jason Yosinski, Jeff Clune, Yoshua Bengio, and Hod Lipson. How transferable are features in deep neural networks? In *Proceedings of the 28th International Conference on Neural Information Processing Systems - Volume 2, NIPS'14*, pages 3320–3328, Cambridge, MA, USA, 2014. MIT Press.
- [99] Ilya Loshchilov and Frank Hutter. SGDR: Stochastic Gradient Descent with Warm Restarts. In *International Conference on Learning Representations*, 2017.
- [100] Lutz Prechelt. Early Stopping - But When? In *Neural Networks: Tricks of the Trade*, pages 55–69. Springer Berlin Heidelberg, Berlin, Heidelberg, 1998.
- [101] Marcel Berger. *A panoramic view of Riemannian geometry*. Springer, 2003.
- [102] Laurent Najman and Pascal Romon, editors. *Modern Approaches to Discrete Curvature*, volume 2184 of *Lecture Notes in Mathematics*. Springer International Publishing, 2017.
- [103] Melanie Weber, Emil Saucan, and Jürgen Jost. Characterizing complex networks with forman-ricci curvature and associated geometric flows. *Journal of Complex Networks*, 5(4):527–550, 2017.
- [104] Melanie Weber, Emil Saucan, and Jürgen Jost. Can one see the shape of a network? *arXiv preprint arXiv:1608.07838*, 2016.
- [105] Tanima Chatterjee, Réka Albert, Stuti Thapliyal, Nazanin Azarhooshang, and Bhaskar DasGupta. Detecting network anomalies using forman-ricci curvature and a case study for human brain networks. *Scientific reports*, 11(1):8121, 2021.
- [106] Zhiqiang Zhong, Cheng-Te Li, and Jun Pang. Hierarchical message-passing graph neural networks. *Data Mining and Knowledge Discovery*, 37(1):381–408, 2023.
- [107] Vincent D Blondel, Jean-Loup Guillaume, Renaud Lambiotte, and Etienne Lefebvre. Fast unfolding of communities in large networks. *Journal of Statistical Mechanics: Theory and Experiment*, 2008(10):P10008, 2008.

SUPPLEMENTARY INFORMATION

COMPUTATIONAL PROCEDURE FOR PERIODIC DISTANCE MATRIX CONSTRUCTION

Algorithm 1: Construction of the Periodic Distance Matrix

Input: Molecular structure of a single repeating unit

Part I: Generation of translated repeating units

- 1: Identify backbone path between terminal dummy atoms
 - 2: Fragment along backbone bonds that are not part of rings
 - 3: Generate all cyclic permutations of backbone fragments
 - 4: Remove duplicate structures to obtain K unique repeating units
 - 5: **for** $k = 1$ to K **do**
 - 6: Generate 3D coordinates $\{e_\alpha^{(k)}\}_{\alpha=1}^N$ using Universal Force Field
 - 7: **end for**
-

Part II: Periodic distance matrix computation

- 8: **for** $\alpha = 1$ to N **do**
 - 9: **for** $\beta = 1$ to N **do**
 - 10: $D_{\alpha\beta} \leftarrow \min_k \|e_\alpha^{(k)} - e_\beta^{(k)}\|$
 - 11: **end for**
 - 12: **end for**
-

Output: Periodic distance matrix \mathbf{D}

MATHEMATICAL BACKGROUND ON SIMPLICIAL COMPLEXES AND VIETORIS–RIPS FILTRATION

Simplicial complexes

Let V be a finite set. A *simplicial complex* K on V is a collection of non-empty subsets of V satisfying:

1. If $\sigma \in K$ and $\tau \subseteq \sigma$, then $\tau \in K$.
2. For every $v \in V$, the singleton $\{v\}$ belongs to K .

The elements of V are called *vertices*, and the elements of K are called *simplices*. A simplex $\sigma \in K$ containing $p + 1$ vertices is called a *p-simplex* and is said to have dimension p . If $\tau \subseteq \sigma$, then τ is called a *face* of σ . The set of all p -simplices of K is denoted by K_p . The dimension of K is the maximum dimension among its simplices.

Simplicial complexes provide a combinatorial framework for encoding higher-order relationships. Vertices represent individual entities, edges represent pairwise relations, triangles encode three-body interactions, and higher-dimensional simplices capture multi-body interactions.

Vietoris–Rips complex

Let $S = \{1, 2, \dots, N\}$ be a finite set, and let

$$\mathbf{D} \in \mathbb{R}_{\geq 0}^{N \times N}$$

be a symmetric distance matrix with $\mathbf{D}_{\alpha\alpha} = 0$ for all $\alpha \in S$. For a threshold $\epsilon > 0$, the *Vietoris–Rips complex* at scale ϵ , denoted $\text{VR}_\epsilon(\mathbf{D})$, is defined as

$$\text{VR}_\epsilon(\mathbf{D}) = \{\sigma \subseteq S \mid \mathbf{D}_{\alpha\beta} \leq \epsilon \text{ for all } \alpha, \beta \in \sigma\}.$$

Thus:

- A vertex $\{\alpha\}$ is always included.
- An edge $\{\alpha, \beta\}$ is included if $\mathbf{D}_{\alpha\beta} \leq \epsilon$.
- A p -simplex arises whenever all pairwise distances among $p + 1$ vertices are at most ϵ .

The Vietoris–Rips complex depends only on pairwise distances and provides a combinatorial construction of higher-order structure directly from a distance matrix.

Filtration of Vietoris–Rips complexes

Given a distance matrix \mathbf{D} , the Vietoris–Rips construction admits a natural filtration obtained by varying the threshold parameter ϵ . Specifically, one may consider the family of complexes

$$\text{VR}_\epsilon(\mathbf{D}), \quad \epsilon \geq 0,$$

which satisfies

$$\text{VR}_\epsilon(\mathbf{D}) \subseteq \text{VR}_{\epsilon'}(\mathbf{D}) \quad \text{whenever } \epsilon \leq \epsilon'.$$

Since the vertex set S is finite, the distance matrix \mathbf{D} contains only finitely many distinct pairwise distances. Consequently, new simplices can appear only when ϵ crosses one of these distance values. The Vietoris–Rips construction therefore induces a finite canonical filtration, in which simplices are added at discrete critical thresholds determined entirely by \mathbf{D} . This canonical filtration describes how the combinatorial structure evolves as increasingly longer-range interactions are permitted.

In practice, however, it is often unnecessary to use all critical distance values. In this work, we utilize a coarse, chemically motivated filtration by selecting a small number of fixed cutoff distances, namely 2 Å, 3 Å, and 4 Å. These thresholds correspond to short range (covalent) and long range (non-covalent) interaction ranges and provide a principled multiscale representation suited to molecules.

FORMAN CURVATURE

Forman introduced a discrete notion of Ricci curvature [44] derived from a combinatorial analogue of the classical Bochner–Weitzenböck formula in Riemannian geometry. In the smooth setting, the Bochner–Weitzenböck formula establishes a fundamental relationship between curvature and the Riemannian Laplace operator [101–103]. Although originally formulated for *weighted CW cell complexes*, Forman’s definition extends naturally to polyhedral complexes, simplicial complexes, and graphs, all of which are special instances of cell complexes [44, 104].

In Riemannian geometry, the Bochner–Weitzenböck formula decomposes the Laplace operator acting on p -forms as

$$\square_p = (\nabla_p)^* \nabla_p + F_p,$$

where \square_p denotes the Laplace operator on p -forms over a compact Riemannian manifold \mathcal{M} , ∇_p is the covariant derivative, and F_p is a zeroth-order operator whose value at a point $x \in \mathcal{M}$ depends only on local derivatives of the metric tensor.

Forman demonstrated that an analogous decomposition can be constructed in the discrete setting:

$$\square_p = B_p + F_p,$$

where \square_p now represents the *combinatorial Riemann–Laplace operator*, B_p is the *combinatorial Bochner (or rough) Laplacian*, and F_p defines the *p*th *combinatorial curvature operator*. For any *p*-cell α , Forman defined the curvature function

$$\mathcal{F}_p(\alpha) = \langle F_p(\alpha), \alpha \rangle.$$

While \mathcal{F}_p does not admit a direct geometric interpretation in the smooth setting for $p > 1$, the case $p = 1$ coincides with Ricci curvature. Thus, the *Forman–Ricci curvature* of a 1-cell (edge) e is given by $\mathcal{F}_1(e)$. This construction applies generally to weighted cell complexes.

Computation on simplicial complexes

For a weighted simplicial complex \mathcal{K} , the combinatorial Bochner–Weitzenböck framework assigns a curvature value $\mathcal{F}_p(\sigma)$ to each *p*-simplex $\sigma \in \mathcal{K}$. In particular, when $p = 1$, the quantity $\mathcal{F}_1(\sigma)$ provides a discrete analogue of classical Ricci curvature on edges.

Two *p*-simplices $\sigma_1, \sigma_2 \in \mathcal{K}_p$ are said to be *parallel*, written $\sigma_1 \parallel \sigma_2$, if exactly one of the following conditions holds: 1. There exists a $(p + 1)$ -simplex $\tau \in \mathcal{K}_{p+1}$ such that $\sigma_1, \sigma_2 \subset \tau$, or 2. There exists a $(p - 1)$ -simplex $\eta \in \mathcal{K}_{p-1}$ such that $\eta \subset \sigma_1, \sigma_2$. That is, two simplices of equal dimension are parallel if they share either a common coface or a common face, but not both. The set of parallel simplices of σ is denoted $\text{Parallel}(\sigma)$.

The Forman–Ricci curvature of an edge (1-simplex) $e \in \mathcal{K}_1$ is defined as

$$\kappa_F(e) = w_e \left[\left(\sum_{f \in \text{Coface}(e)} \frac{w_e}{w_f} + \sum_{v \in \text{Face}(e)} \frac{w_v}{w_e} \right) - \sum_{\hat{e} \in \text{Parallel}(e)} \left| \sum_{f \in \mathcal{K}_2: \hat{e}, e \subset f} \frac{\sqrt{w_e w_{\hat{e}}}}{w_f} - \sum_{v \in \mathcal{V}: v \subset \hat{e}, e} \frac{w_v}{\sqrt{w_e w_{\hat{e}}}} \right| \right],$$

where w_σ denotes the weight assigned to simplex σ .

In the unweighted case, where $w_\sigma = 1$ for all $\sigma \in \mathcal{K}$, the curvature simplifies to a purely combinatorial expression:

$$\kappa_F^\#(e) = \#\text{Face}(e) + \#\text{Coface}(e) - \#\text{Parallel}(e).$$

This formulation has been applied to various types of abstract simplicial complexes, including clique complexes derived from networks [67, 105] and Vietoris–Rips complexes constructed from point cloud data [70].

More generally, Forman’s framework provides a principled method to define curvature for simplices of arbitrary dimension. For any weighted simplicial complex \mathcal{K} , the combinatorial Bochner–Weitzenböck formula defines a curvature function $\mathcal{F}_p(\sigma)$ for each *p*-simplex $\sigma \in \mathcal{K}$. The case $p = 1$ recovers the discrete Ricci curvature on edges, while higher-dimensional analogues depend on the weights of faces, cofaces, and parallel simplices. In the unweighted setting, the curvature reduces to the combinatorial form

$$\mathcal{F}_p^\#(\sigma) = \#\text{Face}(\sigma) + \#\text{Coface}(\sigma) - \#\text{Parallel}(\sigma),$$

which directly generalizes the edge-based Ricci curvature expression to arbitrary simplices. For a comprehensive treatment of Forman curvature on weighted complexes, we refer the reader to Forman’s original work [44].

COMPARISON OF HSMP WITH HIERARCHICAL MESSAGE-PASSING GNNs

Hierarchical Message-Passing Graph Neural Networks have been previously introduced [106] to address two limitations of flat message-passing GNNs, namely the inability to capture long-range interactions and the failure to encode multi-resolution graph semantics. In such a framework, nodes are organized into a multi-level hierarchy of super-graphs, where each super-node at level t represents a cluster of nodes from level $t - 1$. Super-nodes are typically constructed using community detection algorithms such as Louvain [107]. Message passing then proceeds via

three propagation schemes to aggregate information across hierarchical levels, namely bottom-up, within-level, and top-down.

Below, we discuss how HSMP fundamentally differs from hierarchical message-passing GNNs in terms of motivation and underlying mechanisms. An illustration comparing the two approaches is provided in Figure S3.

Graphs vs. Simplicial Complexes Hierarchical MPGNNs operate exclusively on graphs, where message passing is restricted to pairwise interactions along edges. HSMP, by contrast, operates on simplicial complexes, where simplices of dimension k encode simultaneous interactions among $k + 1$ atoms. This places HSMP within the framework of topological deep learning, enabling it to explicitly represent many-body interactions that are inaccessible to graph-based approaches.

Absence of Super-nodes Across Levels In hierarchical MPGNNs, each level of the hierarchy introduces a distinct, smaller set of super-nodes formed by collapsing groups of lower-level nodes. Hence, the node sets at different levels are disjoint. In the context of molecular data, higher-level nodes might lack a direct chemical interpretation. In HSMP, the node set remains identical across all filtration levels. Every node corresponds to a specific atom in the repeating unit. The hierarchy in HSMP encodes spatial scale, specifically, the filtration parameter ϵ_i controls the range of interactions, progressing from covalent bonds to non-covalent interactions.

Task-specific Interpretation of Hierarchy The hierarchical structure in hierarchical MPGNNs is typically derived from community detection on the graph, which is often task-agnostic and may lack inherent physical meaning. In HSMP, the hierarchy is defined by a Vietoris–Rips filtration over a distance matrix, where each level corresponds to a chemically meaningful interaction range. This ensures that the hierarchy directly reflects the spatial structure of the polymer.

Cross-scale Information Flow Hierarchical MPGNNs propagate information across levels through explicit bottom-up and top-down message passing between the original nodes and their associated super-nodes. In HSMP, information flows across scales through the Cross-Scale Refinement (CSR) module, which uses the representation of a simplex at a coarser scale to modulate its representation at a finer scale. Since the nested structure of Vietoris–Rips complexes guarantees that every simplex present at ϵ_i also exists at ϵ_{i+1} , this cross-scale transfer is well-defined for every simplex without requiring a clustering step.

Compatibility with Molecular Pretraining A practical implication of the design choices behind HSMP is that at the finest filtration level ($\epsilon_1 = 2 \text{ \AA}$), the simplicial complex reduces to the covalent bond graph of the polymer. Node representations at this scale are enriched by higher-order and multi-scale information propagated from coarser levels via CSR, and the resulting graph is structurally compatible with standard molecular graph pretraining frameworks. HSMP can therefore serve as a direct replacement for graph-based self-supervised pretraining, as readout is performed exclusively at the molecular graph level. In contrast, frameworks such as hierarchical MPGNNs require pooling across multiple levels with distinct, disjoint node sets.

BASELINE MODEL CONFIGURATIONS

All baseline models were evaluated using the same predefined five-fold cross-validation splits as Periodic-TDL. For each fold, 80% of the data was used for training and 20% for testing, with 20% of the training portion reserved for validation. Validation RMSE was used for model selection. Unless otherwise specified, official pretrained weights and default hyperparameters from the original implementations were used without additional tuning or architectural modification.

Morgan (NN). Extended-connectivity circular fingerprints (ECFP4; radius 2, 1024 bits) were computed using RDKit from canonical SMILES strings. Bit-based fingerprints were used. The resulting vectors were input to a three-layer multilayer perceptron (hidden dimension 1024, ReLU activation, dropout 0.2) with a final linear regression layer. Models were trained using AdamW with learning rate 3×10^{-4} and weight decay 0.05 for up to 100 epochs. No task-specific tuning was performed.

polyBERT. The pretrained polyBERT transformer released by the original authors was finetuned for each downstream task. Canonical SMILES strings were tokenized using the official tokenizer, with polymer anchor symbols normalized to match the pretraining convention. The representation corresponding to the [CLS] token was used as input to a regression head. Finetuning followed a two-stage protocol in which the head was trained prior to joint

optimization with the backbone using separate learning rates. Targets were standardized using statistics computed from the training split and inverse-transformed for evaluation.

TransPolymer. The pretrained TransPolymer checkpoint provided in the official repository was finetuned using the base configuration specified by the authors. No architectural modifications were introduced. Finetuning was performed under the same cross-validation splits as Periodic-TDL, with early stopping based on validation performance.

polyGNN. The polyGNN architecture was implemented using the official library. Polymer graphs were constructed using the monocycle featurization scheme provided by the original implementation. A single-task model was trained independently for each property using the default feature configuration. Training was performed using mean squared error loss without ensembling or hyperparameter optimization.

MolCLR (GCN and GIN). Pretrained MolCLR encoders with both GCN and GIN backbones were finetuned for each downstream property without architectural modification. The original configuration provided in the repository was used for optimization and scheduling. Both backbone variants were trained independently under the same data splits and evaluation protocol.

TransChem. The TransChem architecture was initialized from the pretrained checkpoint released by the authors. RDKit descriptors were computed according to the feature specification described in the original Supplementary Information and combined with sequence representations as defined in the official implementation. Finetuning followed the base configuration provided in the repository without additional hyperparameter tuning.

MMPolymer. The MMPolymer model was initialized from the pretrained weights released by the original authors and finetuned using the default hyperparameter configuration. No architectural modifications or additional tuning were introduced. Evaluation was conducted under the same cross-validation splits as Periodic-TDL.

ABLATION STUDIES

Effect of periodic representation and hierarchical message passing

To evaluate the effect of the periodic Rips complex representation and hierarchical message passing, we performed an ablation study where these components are selectively removed. The periodic representation treats the polymer as an extended system utilizing a periodic distance matrix, thereby encoding interactions between atoms belonging to adjacent repeating units. In contrast, the non-periodic representation restricts all interactions to atoms within a single monomer. Hierarchical message passing includes multi-scale propagation of information across filtration levels, where features are refined from coarser to finer scales via cross-scale refinement modules. Within each filtration level, message passing is first performed over edges using upper adjacencies and co-boundary adjacencies, followed by node-level message passing informed by the updated edge representations. In the non-hierarchical setting, message passing is restricted to within-scale interactions only, without any cross-scale refinement. Specifically, edge-edge and node-node message passing are performed independently at each cutoff, and the resulting features are pooled and concatenated to obtain the final polymer representation.

All results for this ablation study are summarized in Table S3, which reports the RMSE and R^2 values for three models across all target properties. These models are constructed from the HSMP architecture with selective removal of components: (i) the full model with both periodic representation and hierarchical message passing, (ii) the model without periodic representation but with hierarchical message passing, and (iii) the model with periodic representation but without hierarchical message passing. All three models were trained under identical conditions to ensure a fair comparison. In particular, we restricted all models to single-head simplicial message passing, removed any effects of pretraining, and keep all training hyperparameters fixed. This controlled setup isolates the impact of periodicity and hierarchical propagation on downstream performance.

Effect of multi-head message passing, pretraining, and model capacity

To evaluate the effect of multi-head simplicial message passing, pretraining, and model capacity, we performed an ablation study where these components are selectively varied. Multi-head message passing decomposes feature propagation into multiple simplicial message passing heads. In contrast, the single-head model restricts message passing to a single channel, limiting the diversity of learned representations. Pretraining initializes the model using

a large corpus of polymer structures, allowing it to learn transferable chemical and structural features prior to downstream fine-tuning. In the absence of pretraining, model parameters are randomly initialized and learned solely from the supervised training data. Model capacity is controlled through the hidden dimension, with reduced-capacity models employing smaller hidden dimensions.

All configurations considered in this study are summarized in Table S4, which reports architectural details including hidden dimension, number of heads, pretraining data size, and the number of trainable parameters. The evaluated models correspond to variations of the HSMP architecture with controlled modifications: (i) MH-Base (Pretrained), the full model with multi-head message passing and pretraining, (ii) MH-Base (Random), which removes pretraining while retaining the same architecture, (iii) SH-Base (Pretrained), which replaces multi-head message passing with a single-head version at fixed capacity, (iv) MH-Small (Pretrained), which reduces model capacity while retaining multi-head message passing and pretraining, and (v) SH-Small (Pretrained), which combines reduced capacity with single-head message passing.

All models were trained under identical conditions to ensure a fair comparison. In particular, we keep the periodic representation and hierarchical message passing fixed across all models, and maintain identical training hyperparameters. This controlled setup isolates the impact of multi-head message passing, pretraining, and model capacity on downstream performance. The corresponding performance improvements relative to the best baseline model for each dataset and metric are reported in Table S5, enabling a direct comparison of how each design choice across model configurations contributes to predictive performance.

SYNTHESIS AND CHARACTERIZATION OF POLY(2-(ACRYLOYLOXY)ETHYL BENZOATE), POLY(2-(METHACRYLOYLOXY)ETHYL BENZOATE), AND POLY(2-ACRYLAMIDOETHYL BENZOATE)

Materials Benzoic acid (98%, Sigma Aldrich, USA), 2-hydroxyethyl methacrylate (HEMA) (>95%, Tokyo Chemical Industry (TCI), Japan), 2-hydroxyethyl acrylate (HEA) (>95%, Tokyo Chemical Industry (TCI), Japan), 2-hydroxyethyl acrylamide (HEAm) (>95%, Sigma Aldrich, Japan), 4-dimethylaminopyridine (DMAP) ($\geq 99\%$, Sigma Aldrich), 1-(3-dimethylaminopropyl)-3-ethylcarbodiimide hydrochloride (EDC·HCl) (>98%, TCI), N,N'-dicyclohexylcarbodiimide (DCC) (99%, Sigma Aldrich), hydrogen peroxide solution (35% in water) (TCI), 2,2'-azoisobutyronitrile (AIBN) (95%, Fujifilm Wako Pure Chemical, Japan), dichloromethane (DCM) (99.8%, Fisher Chemicals, USA), anhydrous 1,4-dioxane (99.8%, Sigma Aldrich), and N,N-dimethylformamide (DMF) (>99.5%, TCI) were used as received.

Synthesis of 2-(Methacryloyloxy)ethyl benzoate A reaction mixture of 10.00 g (7.68×10^{-2} mol) 2-hydroxyethyl methacrylate, 14.73 g (7.68×10^{-2} mol) 1-ethyl-3-(3-dimethylaminopropyl)carbodiimide hydrochloride (EDC·HCl), and 1.70 g (1.71×10^{-2} mol) 4-(dimethylamino)pyridine (DMAP) was dissolved in 100 mL dichloromethane. The mixture was stirred for 30 min at room temperature, after which 8.53 g (6.98×10^{-2} mol) benzoic acid was added. The reaction was stirred for 16 h at room temperature. The mixture was then washed three times with 150 mL H₂O. The organic phase was washed once more with 100 mL brine and dried over MgSO₄. The solvent was removed to obtain a pale yellow liquid. Yield: 9.53 g (40.6%). ¹H NMR (CDCl₃, 400 MHz): δ 8.04 (d, 2H), 7.55 (t, 1H), 7.43 (t, 2H), 6.14 (s, 1H), 5.57 (s, 3H), 4.53 (m, 4H), 1.94 (s, 3H).

Synthesis of 2-(Acryloyloxy)ethyl benzoate A reaction mixture of 10.00 g (8.61×10^{-2} mol) 2-hydroxyethyl acrylate, 9.56 g (7.86×10^{-2} mol) EDC·HCl, and 1.91 g (1.57×10^{-2} mol) DMAP was dissolved in 100 mL dichloromethane. The mixture was stirred for 30 min at room temperature, followed by the addition of 9.56 g (7.82×10^{-2} mol) benzoic acid. The reaction was stirred for 16 h at room temperature. The mixture was then washed three times with 150 mL H₂O. The organic phase was washed once more with 100 mL brine and dried over MgSO₄. The solvent was removed to obtain a pale yellow liquid. Yield: 10.61 g (48.2%). ¹H NMR (CDCl₃, 400 MHz): δ 7.99 (d, 2H), 7.48 (t, 1H), 7.36 (t, 2H), 6.36 (d, 1H), 6.09 (q, 1H), 5.77 (d, 1H), 4.46 (m, 4H).

Synthesis of 2-acrylamidoethyl benzoate A reaction mixture of 10.00 g (8.68×10^{-2} mol) 2-hydroxyethyl acrylamide, 9.64 g (8.68×10^{-2} mol) EDC·HCl, and 1.93 g (1.58×10^{-2} mol) DMAP was dissolved in 100 mL dichloromethane. The mixture was stirred for 30 min at room temperature, after which 9.64 g (7.90×10^{-2} mol) benzoic acid was added. The reaction was stirred for 16 h at room temperature. The mixture was then washed three times with 150 mL H₂O. The organic phase was washed once more with 100 mL brine and dried over MgSO₄. The solvent was removed to obtain a white solid. Yield: 9.82 g (44.8%). ¹H NMR (CDCl₃, 400 MHz): δ 8.06 (d, 2H), 7.60 (t, 1H), 7.47 (t, 2H), 6.31 (d, 1H), 6.14 (q, 1H), 5.67 (d, 1H), 4.47 (t, 2H), 3.76 (q, 2H), 1.79 (br, 1H).

Synthesis of polymers Homopolymers were synthesized via radical polymerization. A mixture of monomer (typically 2 g), AIBN (typically 0.014 g), and 4.5 g DMF in a Schlenk flask was heated at 70 °C for 20 h under an argon atmosphere with magnetic stirring. The polymer was purified via reprecipitation in diethyl ether (non-solvent) three times and dried overnight under vacuum. The polymerization results are given in Table S8.

Gel permeation chromatography (GPC) GPC analysis was performed using DMF as the eluent on a Shimadzu i-Series Plus liquid chromatograph LC-2030C Plus (Kyoto, Japan) equipped with two Shodex LF-804 columns (300 × 8.0 mm; bead size = 6 μm; pore size = 3000 Å) and one Shodex KD-802 column (300 × 8.0 mm; bead size = 6 μm; pore size = 150 Å). The DMF eluent contained 10 mM LiBr, and the flow rate was 0.34 mL/min (40 °C). Sample detection was conducted using a Shimadzu differential refractometer detector RID-20A, and the column system was calibrated with standard poly(methyl methacrylate)s (PMMA)s.

NMR spectroscopy ¹H NMR and ¹³C NMR spectra were recorded on a Bruker BBFO400 spectrometer (400 MHz) at ambient temperature. Chloroform-*d* (CDCl₃) (Cambridge Isotope Laboratories, USA) or DMSO-*d*₆ (Cambridge Isotope Laboratories) was used as the NMR solvent. Chemical shifts were calibrated using the residual undeuterated solvent or tetramethylsilane (TMS) as an internal standard. Monomer conversions in the polymerization were determined using ¹H NMR from the decay in the peak areas of the vinyl groups of the monomers.

Differential scanning calorimetry (DSC) The glass transition temperatures (T_g) of the three polymers were obtained using differential scanning calorimetry (DSC), specifically a QSeries DSC Q50 model device (TA Instruments, New Castle, USA). DSC analysis was conducted using aluminium sample pans under nitrogen flow at 50 mL/min. Samples were cooled to -60 °C and heated to 200 °C at a heating rate of 10 °C/min.

SUPPLEMENTARY FIGURES

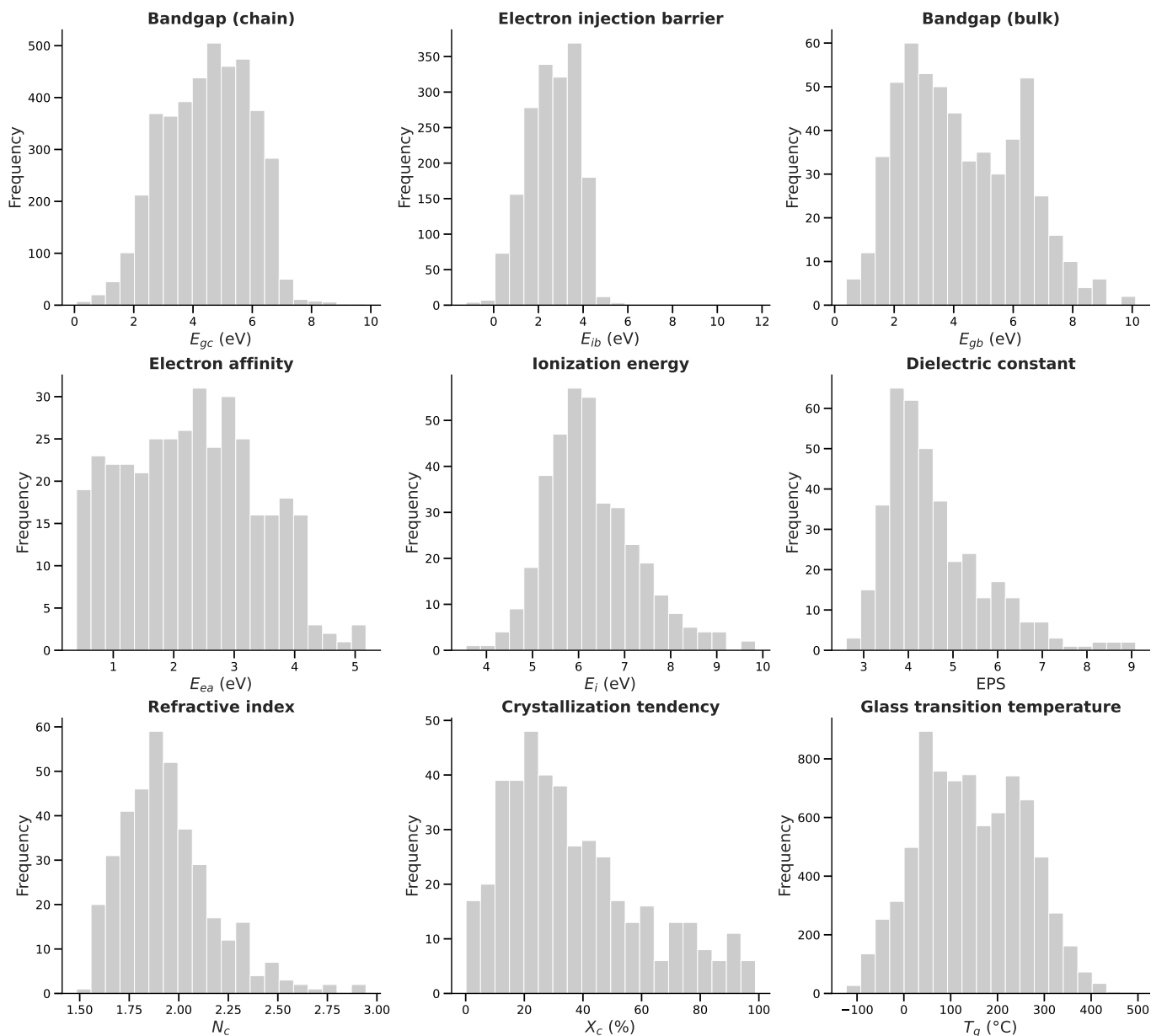


FIG. S1. Distributions of true target values for the nine downstream polymer property prediction tasks evaluated in this work. Histograms are shown for electronic (E_{gc} , E_{ib} , E_{gb} , E_{ea} , E_i), optical (EPS, N_c), physical (X_c), and thermal (T_g) properties. The horizontal axis in each panel corresponds to the property value (with units indicated), and the vertical axis corresponds to the frequency of occurrences within the corresponding bin.

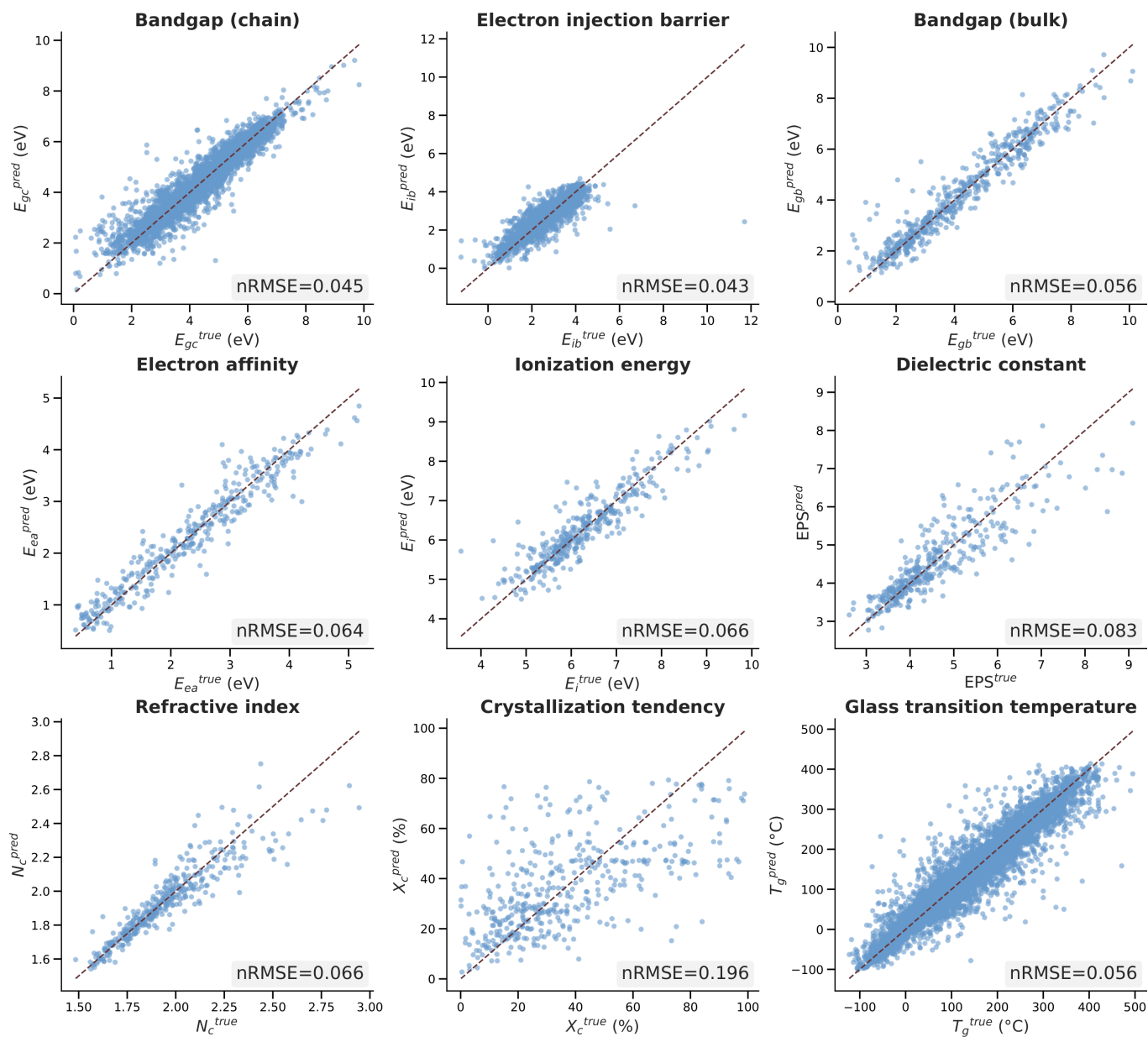


FIG. S2. Parity plots comparing true versus predicted values from Periodic-TDL for all test samples across five cross-validation folds and nine downstream polymer property tasks. Each panel corresponds to one property target. Points are pooled across test folds, and the dashed line indicates a perfect agreement between predicted and true values. Normalized RMSE values are shown in the individual plot panels.

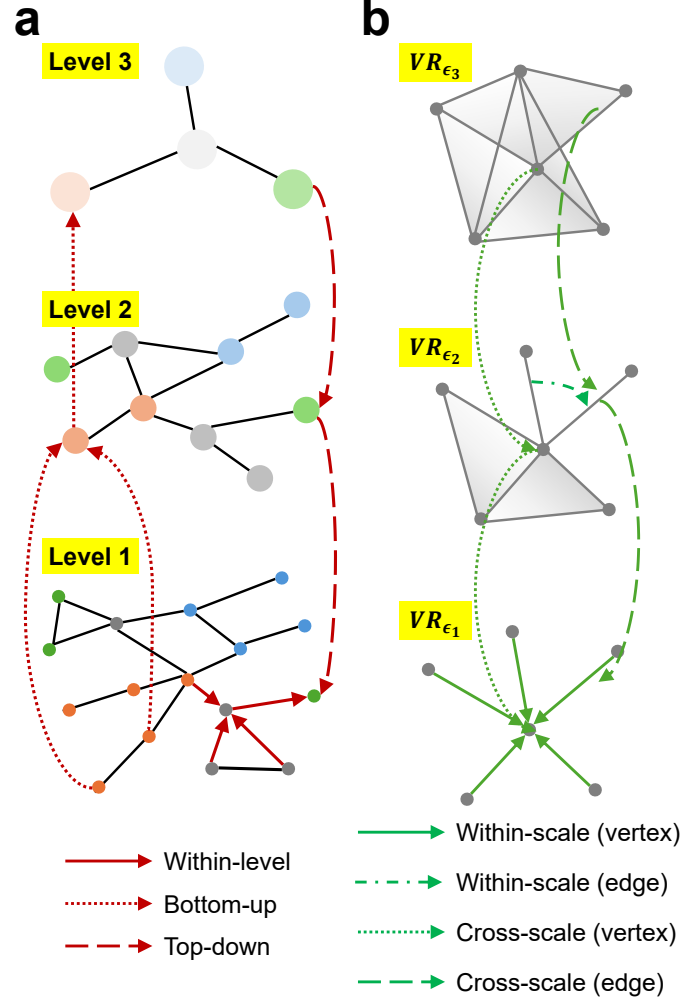


FIG. S3. **Comparison of information flow in Hierarchical MPGNNs and HSMP.** (a) Hierarchical Message-Passing GNN. The hierarchy is constructed by clustering nodes into disjoint sets of super-nodes across Level 1 to Level 3. Information is propagated via bottom-up (dotted red), top-down (dashed red), and within-level message passing. (b) Hierarchical Simplicial Message Passing (HSMP). The hierarchy is defined by a nested Vietoris-Rips filtration ($VR_{\epsilon_1} \subset VR_{\epsilon_2} \subset VR_{\epsilon_3}$) where the node set remains identical across scales. Information flows within-scale (solid green) and across scales (dotted/dashed green) via a cross-scale refinement (CSR) mechanism, where higher-order topological features at coarser scales modulate representations at finer scales.

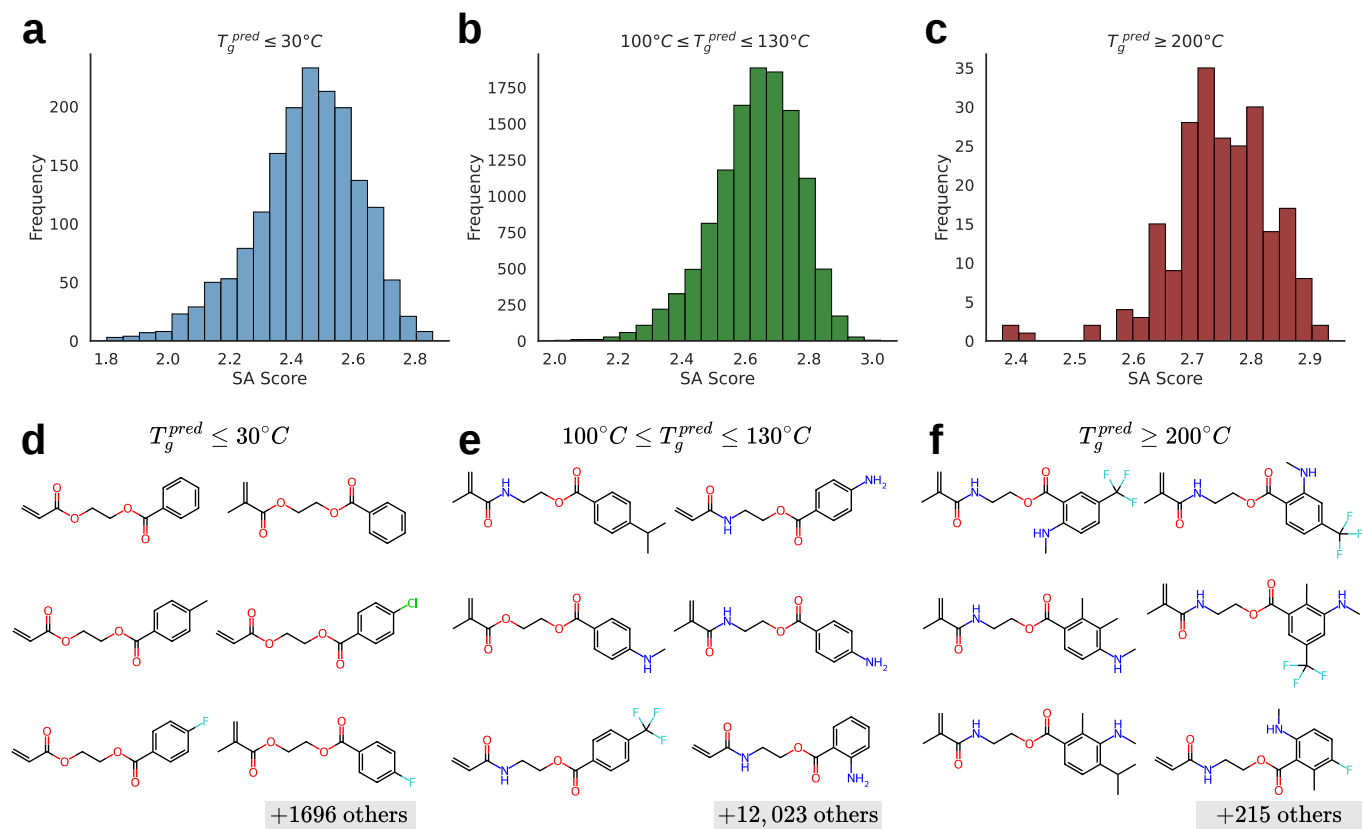


FIG. S4. **Synthetic accessibility of monomers corresponding to polymers in different predicted glass transition temperature ranges.** (a–c) Distributions of Schuffenhauer synthetic accessibility (SA) scores for monomers corresponding to polymers with low ($T_g^{\text{pred}} \leq 30^\circ\text{C}$), medium ($100^\circ\text{C} \leq T_g^{\text{pred}} \leq 130^\circ\text{C}$), and high ($T_g^{\text{pred}} \geq 200^\circ\text{C}$) glass transition temperature ranges, respectively. (d–f) Representative monomers from each T_g^{pred} range, showing the six monomers with the lowest SA scores within each range. These ranges contain 1,702, 12,029, and 221 polymers, respectively. Higher T_g^{pred} ranges are associated with bulkier, more polar and hydrogen-bonding prone polymers.

SUPPLEMENTARY TABLES

TABLE S1. **Summary statistics of the nine downstream polymer property prediction datasets.** For each target, we report the number of samples (n), mean, standard deviation (SD), minimum, maximum, and empirical range ($\max - \min$). These statistics are used to compare RMSE with the standard deviation of each dataset and to compute normalized RMSE, defined as $\text{RMSE}/(\max(y) - \min(y))$, as reported in the Results. Electronic (E_{gc} , E_{ib} , E_{gb} , E_{ea} , E_i), optical (EPS, N_c), and physical (X_c) properties are derived from density functional theory calculations, whereas T_g corresponds to experimentally measured values.

Property	Property name	Class	Unit	n	Mean	SD	Min	Max	Range
E_{gc}	Bandgap (chain)	Electronic	eV	4124	4.488	1.442	0.071	9.835	9.764
E_{ib}	Electron injection barrier	Electronic	eV	1744	2.636	1.107	-1.234	11.703	12.937
E_{gb}	Bandgap (bulk)	Electronic	eV	561	4.242	1.954	0.391	10.114	9.723
E_{ea}	Electron affinity	Electronic	eV	368	2.307	1.089	0.394	5.178	4.785
E_i	Ionization energy	Electronic	eV	370	6.268	0.991	3.558	9.839	6.281
EPS	Dielectric constant	Optical	–	382	4.586	1.119	2.610	9.090	6.480
N_c	Refractive index	Optical	–	382	1.947	0.240	1.484	2.945	1.460
X_c	Crystallization tendency	Physical	%	430	36.76	23.71	0.13	98.81	98.68
T_g	Glass transition temperature	Thermal	°C	7957	145.87	110.50	-123.00	495.00	618.00

TABLE S2. Test R^2 (mean \pm std) for Periodic-TDL and baseline models across nine downstream polymer property prediction tasks. Higher values indicate better performance. Results are computed on identical data splits using five-fold cross-validation. Best and second-best results per target are highlighted in **bold** and underline, respectively.

Model	E_{gc}	E_{ib}	E_{gb}	E_{ea}	E_i	EPS	N_c	X_c	T_g
Morgan (NN)	0.849 \pm 0.010	0.662 \pm 0.048	0.802 \pm 0.026	0.840 \pm 0.009	0.439 \pm 0.115	0.552 \pm 0.092	0.497 \pm 0.122	0.320 \pm 0.095	0.882 \pm 0.010
polyBERT	0.887 \pm 0.012	0.730 \pm 0.048	0.895 \pm 0.018	0.904 \pm 0.015	<u>0.794 \pm 0.024</u>	0.674 \pm 0.089	0.768 \pm 0.064	0.298 \pm 0.087	0.889 \pm 0.011
TransPolymer	0.896 \pm 0.016	0.715 \pm 0.053	0.899 \pm 0.032	0.901 \pm 0.017	0.783 \pm 0.028	0.652 \pm 0.080	0.756 \pm 0.058	<u>0.338 \pm 0.073</u>	0.894 \pm 0.014
polyGNN	0.867 \pm 0.020	0.725 \pm 0.048	0.902 \pm 0.027	<u>0.917 \pm 0.018</u>	0.621 \pm 0.188	0.654 \pm 0.157	<u>0.778 \pm 0.074</u>	0.185 \pm 0.142	0.846 \pm 0.005
MolCLR (GCN)	0.850 \pm 0.009	0.725 \pm 0.053	0.875 \pm 0.021	0.867 \pm 0.015	0.693 \pm 0.097	<u>0.675 \pm 0.087</u>	0.745 \pm 0.076	0.238 \pm 0.089	0.835 \pm 0.014
MolCLR (GIN)	0.886 \pm 0.009	<u>0.747 \pm 0.043</u>	0.894 \pm 0.016	0.897 \pm 0.021	0.644 \pm 0.189	0.664 \pm 0.063	0.735 \pm 0.077	0.231 \pm 0.089	0.859 \pm 0.008
TransChem	0.887 \pm 0.017	0.660 \pm 0.104	0.883 \pm 0.034	0.876 \pm 0.038	0.732 \pm 0.120	0.637 \pm 0.100	0.769 \pm 0.049	0.309 \pm 0.039	<u>0.895 \pm 0.010</u>
MMPolymer	<u>0.903 \pm 0.010</u>	0.699 \pm 0.027	<u>0.903 \pm 0.020</u>	0.899 \pm 0.011	0.743 \pm 0.066	0.601 \pm 0.112	0.744 \pm 0.054	0.325 \pm 0.136	<u>0.895 \pm 0.012</u>
Periodic-TDL	0.906 \pm 0.010	0.748 \pm 0.054	0.921 \pm 0.014	0.925 \pm 0.016	0.825 \pm 0.031	0.767 \pm 0.040	0.826 \pm 0.050	0.403 \pm 0.049	0.901 \pm 0.012

TABLE S3. **Effect of periodic representation and hierarchical message passing.** RMSE (\downarrow) and R^2 (\uparrow) values across all target properties for three models defined by the inclusion of periodic representation and hierarchical message passing: periodic + hierarchical, non-periodic + hierarchical, and periodic + non-hierarchical. All models are trained under identical settings with single-head simplicial message passing and without pretraining.

Property	Periodic + Hierarchical		Non-periodic + Hierarchical		Periodic + Non-hierarchical	
	RMSE \downarrow	R^2 \uparrow	RMSE \downarrow	R^2 \uparrow	RMSE \downarrow	R^2 \uparrow
E_{gc}	0.459 \pm 0.027	0.8981 \pm 0.0118	0.464 \pm 0.026	0.8956 \pm 0.0117	0.469 \pm 0.025	0.8935 \pm 0.0125
E_{ib}	0.544 \pm 0.062	0.7563 \pm 0.0400	0.560 \pm 0.053	0.7428 \pm 0.0315	0.551 \pm 0.059	0.7509 \pm 0.0365
E_{gb}	0.549 \pm 0.064	0.9202 \pm 0.0083	0.575 \pm 0.076	0.9125 \pm 0.0126	0.594 \pm 0.082	0.9067 \pm 0.0136
E_{ea}	0.281 \pm 0.034	0.9308 \pm 0.0156	0.299 \pm 0.026	0.9224 \pm 0.0150	0.305 \pm 0.030	0.9190 \pm 0.0186
E_i	0.464 \pm 0.082	0.7756 \pm 0.0290	0.451 \pm 0.064	0.7873 \pm 0.0189	0.448 \pm 0.080	0.7908 \pm 0.0251
EPS	0.580 \pm 0.068	0.7263 \pm 0.0520	0.607 \pm 0.048	0.7010 \pm 0.0420	0.582 \pm 0.067	0.7159 \pm 0.0920
N_c	0.099 \pm 0.006	0.8223 \pm 0.0421	0.110 \pm 0.008	0.7814 \pm 0.0483	0.100 \pm 0.007	0.8189 \pm 0.0472
X_c	18.64 \pm 1.07	0.3746 \pm 0.0721	18.84 \pm 0.82	0.3603 \pm 0.0764	19.36 \pm 1.15	0.3239 \pm 0.0839
T_g	38.11 \pm 1.46	0.8808 \pm 0.0091	38.60 \pm 1.79	0.8776 \pm 0.0120	38.59 \pm 1.06	0.8778 \pm 0.0082

TABLE S4. **Architectural and training details of Periodic-TDL models used in the ablation study.** We report the hidden dimension, number of attention heads, size of the pretraining dataset, and the number of trainable parameters for each model configuration.

Model	Hidden Dim.	# Heads	Pretraining Size	# Parameters
MH-Base (Pretrained)	768	12	\sim 1M	35,019,889
MH-Base (Random)	768	12	0	35,019,889
SH-Base (Pretrained)	768	1	\sim 1M	91,249,205
MH-Small (Pretrained)	512	8	250K	16,792,993
SH-Small (Pretrained)	512	1	250K	40,647,733

TABLE S5. **Relative performance improvement of Periodic-TDL models over best baseline models.** For each dataset, we report the percentage change in test RMSE and the absolute change in test R^2 of different model configurations with respect to the best-performing baseline model for the corresponding metric and dataset. The final row reports the average improvement across all datasets, enabling an overall comparison across model configurations.

Dataset	MH-Base (Pretrained)		MH-Base (Random)		SH-Base (Pretrained)		MH-Small (Pretrained)		SH-Small (Pretrained)	
	RMSE (%) \downarrow	R^2 \uparrow	RMSE (%) \downarrow	R^2 \uparrow	RMSE (%) \downarrow	R^2 \uparrow	RMSE (%) \downarrow	R^2 \uparrow	RMSE (%) \downarrow	R^2 \uparrow
T_g	-2.91	+0.006	-2.77	+0.006	-2.16	+0.005	+5.10	-0.008	+13.69	-0.030
E_{gc}	-1.56	+0.003	+0.22	-0.001	+3.35	-0.007	+5.58	-0.011	+6.92	-0.014
E_{ib}	+0.91	+0.001	+0.18	+0.004	+2.55	-0.007	+4.37	-0.017	-0.91	+0.009
E_{gb}	-8.22	+0.018	-5.03	+0.012	-6.54	+0.015	-0.17	+0.003	+4.19	-0.006
E_{ea}	-4.85	+0.008	-7.44	+0.012	-2.91	+0.003	-2.59	+0.004	+17.48	-0.032
E_i	-8.35	+0.031	+1.35	-0.004	-8.58	+0.032	+4.06	-0.020	+10.16	-0.047
EPS	-14.54	+0.092	-11.34	+0.074	-7.99	+0.048	+2.24	-0.020	-2.56	+0.016
N_c	-10.09	+0.048	-9.36	+0.046	-6.42	+0.037	+6.42	-0.024	+25.69	-0.122
X_c	-5.05	+0.065	-2.55	+0.033	-4.69	+0.056	+3.18	-0.044	+5.05	-0.075
Average	-6.07	+0.030	-4.08	+0.020	-3.71	+0.020	+3.13	-0.015	+8.86	-0.033

TABLE S6. Summary statistics of predicted glass transition temperature (T_g^{pred}) values for the four systematically substituted polymer families. Each family contains polymers generated from 12,052 substituted monomers, with substitutions performed on the phenyl ring. The four families correspond to poly(acrylates) (Ar-Et-A), poly(methacrylates) (Ar-Et-MA), poly(acrylamides) (Ar-Et-AM), and poly(methacrylamides) (Ar-Et-MAM).

Name	Family	Functional group	T_g^{pred} ($^{\circ}\text{C}$)
Ar-Et-A	Poly(acrylate)	Ester	71.51 ± 35.84
Ar-Et-MA	Poly(methacrylate)	Ester	86.93 ± 33.86
Ar-Et-AM	Poly(acrylamide)	Amide	128.48 ± 28.39
Ar-Et-MAM	Poly(methacrylamide)	Amide	141.49 ± 26.59

TABLE S7. **Individual T_g values for literature-based validation pairs.** For the 8 polymers comprising the four literature pairs, we report the polymer abbreviation, full polymer name, experimentally reported T_g , and Periodic TDL-predicted T_g (mean \pm SD across ten cross-validation folds). The ΔT_g values shown in Table 3 are calculated from the individual T_g values for each fold.

Abbreviation	Polymer	T_g^{lit} ($^{\circ}\text{C}$)	T_g^{pred} ($^{\circ}\text{C}$)
Poly-O	poly[N-[4-(methacryloyloxy)phenyl]-2-(4-methoxyphenyl)acetamide]	144.8	157.9 ± 7.7
Poly-A	poly[N-4-[[[(4-methoxyphenyl)acetyl]oxy]phenyl]methacrylamide]	241.8	166.3 ± 8.2
PSA	Poly(syringaldehyde acrylate)	170.0	88.0 ± 10.0
PSMA	Poly(syringaldehyde methacrylate)	180.0	99.1 ± 10.6
PVA	Poly(vanillin acrylate)	95.0	71.2 ± 11.5
PVMA	Poly(vanillin methacrylate)	110.0	88.6 ± 11.3
PGlc- β -EAAM	Poly(N-(beta-glycosyloxy)-ethyl acrylamide)	144.5	106.3 ± 8.3
PGlc- β -EMAAM	Poly(N-(beta-glycosyloxy)-ethyl methacrylamide)	168.0	110.5 ± 7.7

TABLE S8. Polymerization results

Entry	Monomer	$[M]_0/[AIBN]_0$ (equiv.)	T ($^{\circ}\text{C}$)	t (h)	Conv. (%) ^a	M_n ($M_{n,\text{theo}}$) ^{b,c}	D ^b
1	2-(Methacryloyloxy)ethyl benzoate	100/1	70	16	99	25,000 (23,200)	2.48
2	2-(Acryloyloxy)ethyl benzoate	100/1	70	16	99	16,200 (21,800)	2.40
3	2-Acrylamidoethyl benzoate	100/1	70	16	99	46,200 (21,700)	3.33

^a Monomer conversions determined by ^1H NMR. ^b PMMA-calibrated GPC values (DMF eluent). ^c Theoretical M_n calculated according to $([\text{DMDL}]_0/[\text{CTA}]_0) \times (\text{monomer conversion}) \times (\text{molecular weight of DMDL}) + (\text{molecular weight of CTA})$. D denotes dispersity (M_w/M_n).